ACS Catalysis

pubs.acs.org/acscatalysis Research Article

Kinetic Requirements for Selectivity Enhancement During Forced Dynamic Operation of the Oxidative Dehydrogenation of Ethane

Austin Morales, Michael P. Harold,* and Praveen Bollini*

Cite This: ACS Catal. 2024, 14, 7877−7892 Read Online

ACCESS | Metrics & More | Article Recommendations | Supporting Information

ABSTRACT: The viability of alkane oxidative dehydrogenation (ODH) processes specifically, and catalytic partial oxidation reactions more generally, are oftentimes limited by the formation of undesired deep oxidation products such as CO and CO_2. The forced dynamic operation (FDO) of catalytic reactors has been proposed as a means for enhancing desired olefin or oxygenate selectivity and yield over those of CO and CO_2, but an elucidation of the precise mechanistic bases for the dynamic enhancement observed continues to remain evasive. In this work, we provide an explanation of the extent of dynamic enhancement noted during ethane ODH over supported MoO_x catalysts but not VO_x ones—an explanation grounded in a quantitative analysis of the density and reactivity of chemisorbed and lattice oxygen species on these two classes of catalysts. Supported vanadia catalysts, unlike molybdena ones, carry oxygen species with similar reducibilities, resulting in highly contrasting trends in dynamic and steady state ODH properties for the two catalysts. Whereas in the case of VO_x/Al_2O_3, oxygen speciation affects the nature of the hydrocarbon activated (ethane or ethylene), in the case of MoO_x/Al_2O_3, it affects the type of product formed (ethylene or CO_x). Metal oxide loading is shown to be a key parameter impacting dynamic enhancement, with the FDO enhancement of higher loading molybdena samples converging toward that of the vanadia catalyst. The preferential depletion of chemisorbed oxygens is revealed to be a key determinant of the extent of dynamic enhancement, with an asymmetry in modeled O_*/O_L ratios under dynamic conditions relative to SS ones helping rationalize the effect that modulation frequency has on FDO enhancement. Collectively, the results presented here establish a quantitative, molecular-level basis for dynamic enhancement noted during the ODH of ethane, and point to considerations relating to the reactivity of chemisorbed and lattice oxygens as well as their dynamic and steady state ratios as levers for mitigating side-product formation through FDO.

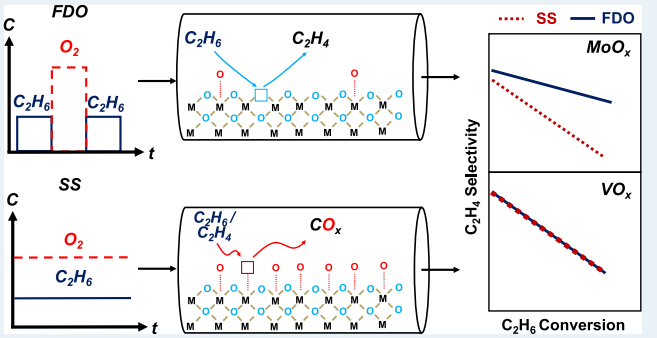

KEYWORDS: *oxidative dehydrogenation, dynamic catalysis, non-steady state, forced dynamic operation, chemisorbed and lattice oxygen*

1. INTRODUCTION

Ethylene is a valuable commodity chemical that is currently produced through the highly endothermic, non-catalytic steam cracking of naphtha and ethane.[1−3] The oxidative dehydrogenation (ODH) of ethane to ethylene on metal oxide catalysts is an attractive exothermic alternative that is energy self-sufficient, and may even be carried out autothermally.[1,4−8] On the other hand, non-selective reactions such as the production of CO, CO_2, or C_2^+ oxygenates limit ODH adoption despite advances in catalyst formulations and reactor designs that mitigate formation of these side products.[6,8−14] Several studies show how the electrophilic nature of gas phase O_2 or chemisorbed oxygen drives non-selective reaction pathways, whereas nucleophilic oxygen stored in the oxide lattice drives selective ODH.[8,11,15,16] Electrophilic chemisorbed oxygen has been proposed to favor the scission of electron-dense C−C and C═C bonds that result in CO_x formation, whereas nucleophilic lattice oxygen has been ascribed the role of cleaving C−H bonds while preserving the C−C bond, thereby resulting in C_2H_4 formation.[8,11,15−17]

In recent years, there has been increased interest in processes that attempt to separate reduction and oxidation half cycles occurring during ODH. Researchers have previously shown that ODH follows Mars−van Krevelen (MvK) redox cycles in which the olefin product is formed during the reduction half cycle and then reoxidized by gas phase oxygen as part of the oxidation half cycle, thereby restoring the oxidation state of the catalyst.[3,4,8] Such separation of reduction and oxidation half cycles helps mitigate undesired interactions that drive nonselective pathways, as shown previously by many

Received: December 13, 2023
Revised: April 18, 2024
Accepted: April 23, 2024
Published: May 6, 2024

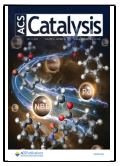

https://doi.org/10.1021/acscatal.3c06066
ACS Catal. 2024, 14, 7877−7892

groups.[5,8,10,13,18,19] For example, the absence of gas phase O_2 has been shown to enhance reaction of C_2H_6 with selective nucleophilic lattice oxygen rather than unselective electrophilic oxygen. Lattice vacancies of the reduced catalyst are expected to be preferentially reoxidized through contact with O_2 in the absence of C_2H_6.[5,8,10,15]

Reactor types proposed to limit byproduct formation by minimizing mixing between the alkane and O_2 include chemical looping, membrane, and circulating fluidized bed reactors,[9−11,15,18−20] with researchers also having aimed to achieve this through catalyst design. Gao et al., for instance, demonstrated the use of promoted core−shell catalysts to enhance selective oxygen exchange during chemical looping ODH.[5] Others, such as Luongo et al., have shown that separating gaseous oxidant and reductant using semipermeable layered catalysts can increase ethylene selectivity.[8] Skoufa et al. evaluated the distributed feed reactor as an alternative to conventional cofeed operation of ethane ODH.[12] Similarly, Waku et al. investigated the use of a membrane reactor for ethane ODH over VO_x/Al_2O_3 catalysts and noted negligible selectivity enhancement for the membrane versus the steady state (SS) cofeed case.[11] The lack of selectivity enhancement was attributed to the selective and nonselective reactions being independent of O_2 concentration;[11] O_2 concentration dependency is known to be a necessary kinetic feature for selectivity enhancement during distributed addition of O_2 in consecutive−parallel reactions.[21] Instead, selectivity enhancement was found to only occur under conditions in which noncatalytic gas phase reactions contribute to the overall chemistry.[11] Others, such as Novotný et al., found significant enhancement during chemical looping of ethane and oxygen over MoO_x/Al_2O_3 catalysts carrying submonolayer molybdena loadings despite the absence of contributions from homogeneous reactions.[19]

Despite the progress made with respect to alternatives to steady state cofeed ODH operation, a precise understanding of the mechanistic underpinnings for improvements in performance, and relationships between the kinetics of specific reaction steps and measured selectivity enhancements remain elusive. This gap in the literature prevents the rational design of catalytic reactors that are operated periodically. Alumina-supported vanadia catalysts are among the most commonly investigated class of materials for ethane and propane ODH, yet forced dynamic operation for this particular application has not, to the best of our knowledge, been evaluated in the open literature. In this study, we develop, in tandem with steady state and transient ODH experiments, transient kinetic models of active oxygen formation and scavenging over two commonly evaluated supported oxide catalysts—VO_x/Al_2O_3 and MoO_x/Al_2O_3. These models lead to a quantitative understanding of the contrasting roles of lattice and chemisorbed oxygen species within MvK cycles occurring over the two catalysts. We identify pertinent kinetic features that provide the basis for dynamic enhancement on MoO_x but not VO_x catalysts, and present the ratio of chemisorbed to lattice oxygen (O_*:O_L) as a salient variable that allows us to rationalize the effect of specific reaction conditions (including frequency, temperature, and O_2 pressure) that help maximize dynamic selectivity enhancement during the oxidative dehydrogenation of ethane.

2. EXPERIMENTAL METHODS

γ-Al_2O_3-supported metal oxide catalysts were synthesized through incipient wetness impregnation. In the case of VO_x on Al_2O_3, approximately 10 mL of deionized (DI) water was used for 5 g of support. Oxalic acid (Sigma-Aldrich) was added to a solution of ammonium metavanadate (Sigma-Aldrich) in water until the pH reached a value of 2.[2,4,16] This step ensured complete dissolution of the precursor. The resulting paste was dried overnight at 120 °C. The sample was subsequently calcined at 600 °C for 6 h with 0.5 L/min of air (99.99% Praxair).[3,4] MoO_x on Al_2O_3 samples were synthesized through impregnation of ammonium heptamolybdate tetrahydrate on γ-Al_2O_3 powder.[19] The resulting paste was left to dry at 120 °C overnight, and the sample calcined in air at 600 °C (99.99% Praxair).[19] MoO_x catalysts were pelletized and sieved between 425 μm and 2 mm for reaction tests. VO_x catalysts were pelletized and sieved between 180 and 425 μm. Larger quantities of catalyst were required to reach higher conversions on the less active MoO_x/Al_2O_3 catalysts;[19] hence, larger diameter pellets were used to minimize pressure drops across the longer MoO_x/Al_2O_3 beds. Kinetic measurements were determined to be independent of mass and heat transport limitations (see List S1 and Table S1 in the Supporting Information).

Flow reactor studies were carried out in a 4 mm ID quartz tube reactor, with temperature control achieved using a tube furnace and measured with thermocouples at the inlet and outlet of the catalyst bed. Catalysts were contacted with 10% O_2 in N_2 at 600 °C for 30 min before each experiment. 3% C_2H_6 in N_2 (Praxair) and O_2 (10% and pure Praxair) concentration feed forcing was performed with two 4-way actuator values from VICI Valco (see Scheme S2 in the Supporting Information). Each valve alternates at a prescribed frequency between reactant (C_2H_6 or O_2) and a separate N_2 feed to maintain an equivalent overall flow rate. Reactants were pulsed with 2 min periods and a 50% duty cycle (1 min on, 1 min off). Examples of reactant concentration profiles versus time are provided in Section S3. Concentrations of O_2, C_2H_6, and CO_2 were measured using a quadrupole mass spectrometer (Hiden Analytical model HPR20) at 32, 30, and 44 m/z, respectively. Relative intensities were used to deconvolute overlapping mass spectra of C_2H_4 from C_2H_6. C_2H_4 and CO concentrations were recorded using a Fourier transform infrared (FTIR) spectrometer gas analyzer (MKS). Equations 1 and 2 were used to determine carbon selectivity and C_2H_6 conversion, respectively.

$$S_i = \frac{\nu_i N_i}{(2N_{C_2H_4} + N_{CO} + N_{CO_2})} \quad (1)$$

$$X_{C_2H_6} = \frac{2N_{C_2H_4} + N_{CO} + N_{CO_2}}{2N^f_{C_2H_6}} \quad (2)$$

where N_i represents the moles of species i and ν_i is the number of carbon atoms in species i.

Catalyst surface areas were determined by applying the Brunauer−Emmett−Teller (BET) equation to N_2 physisorption data measured at 77 K. Before measuring surface areas, catalysts were subjected to overnight degassing at 200 °C to ensure that the sample was free of contaminants. N_2 physisorption isotherms of the samples tested can be found in Section S4. X-ray diffraction (XRD) patterns were measured using an Empyrean Malvern Panalytical X-ray diffractometer with a Cu K alpha source (λ = 0.1542) operating at 40 kV and 45 mA. Diffraction patterns were measured over a 2θ range of 0−90° for 30 min. Further XRD characterization details are

https://doi.org/10.1021/acscatal.3c06066
ACS Catal. 2024, 14, 7877−7892

provided in Section S5. Catalyst reducibility was assessed using CO temperature programed reduction (CO TPR) experiments. Prior to CO TPR, catalysts were contacted with a gas containing 10% O_2 in N_2 for 30 min at 600 °C. The reactor was then cooled to 25 °C under N_2 to purge residual O_2. During CO TPR, catalysts were reduced under a 10% CO in N_2 flow while increasing the bed temperature from 25 to 550 °C at a ramp rate of 10 °C per minute, and the molar flow rate of CO_2 at the outlet of the catalyst bed was quantified using mass spectrometry (see Section S6 for more details). Carbon selectivity as a function of ethane conversion was determined by varying catalyst weight and total flow rate, varying W/F between 0.5 and 10 mg/sccm. Blank tube tests indicated the absence of homogeneous reactions below 600 °C. Presented data had carbon balances of 100 ± 5%. Coke formation rates are assumed to be negligible given the favorable carbon balance values and stable operation over many runs. More specifically, steady state rates and selectivities were found to be unaffected by extended dynamic redox cycling for over 6 months. Error bar estimation and propagation is described in Section S7.

3. RESULTS AND DISCUSSION

3.1. FDO and SSO over VO_x/Al_2O_3. A 3 wt % VO_x/Al_2O_3 catalyst (0.7 nominal monolayer coverage) was compared under SS and periodic (bang−bang modulation; see Figure S3 for typical feed concentration profiles versus time) operation to evaluate the effect of separating the MvK reduction and oxidation half cycles on ethylene selectivity.[3,4,16] Dynamic operation was conducted by alternatingly exposing the catalyst to ethane (reduction) and O_2 (oxidation) for 1 min each, i.e., 2 min period at 50% duty cycle, such that the cyclic (time integral) average reactant concentrations are equivalent to the SS concentrations. For example, a SS feed containing 1% C_2H_6 and 10% O_2 is compared to a dynamic feed switching between 0% C_2H_6 + 20% O_2 and 2% C_2H_6 + 0% O_2 at 50% duty. Catalyst amount and total flow rate were adjusted to determine product selectivity as a function of ethane conversion. Ethane ODH follows a triangular reaction network in which ethylene is formed as an intermediate product that can undergo secondary reactions to form CO_x, which can also be formed through the primary deep oxidation of ethane (Scheme 1).

Scheme 1. Triangular Reaction Network for Ethane ODH over VO_x and MoO_x Catalysts Comprising Selective ODH (r_1) and Unselective Deep Oxidation Reactions (r_2 and r_3)

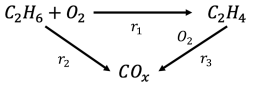

Dynamic operation results in lower cycle-averaged product formation rates and conversions for alkane ODH because active oxygen concentrations in the absence of gas phase O_2 are necessarily lower than in its presence under SS conditions.[11,12,15,20] In order to compare product selectivities at the same ethane conversion, higher residence times are needed under FDO compared to SSO.

Figure 1 shows the ethylene selectivity (C basis) as a function of ethane conversion at 1 and 10% O_2 during periodic and SSO over the 0.7 ML VO_x catalyst at 550 °C. A full plot of carbon selectivity versus conversion for all products (ethylene, CO, and CO_x) is provided in Section S8. Ethylene selectivity decreases with increasing ethane conversion, indicating that

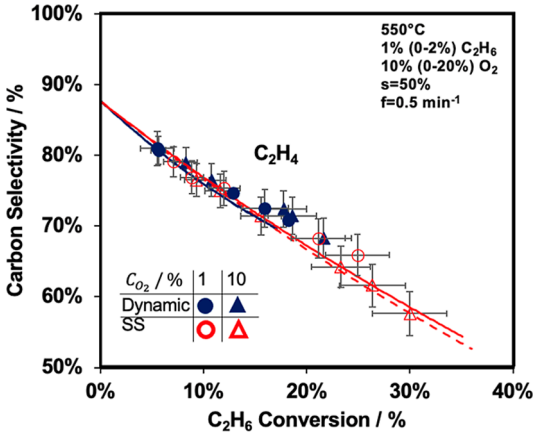

Figure 1. Dynamic and SS C_2H_4 carbon selectivities [%] as a function of C_2H_6 conversion [%] with 1% C_2H_6 and either 1 or 10% O_2 over 0.7 ML VO_x/Al_2O_3. Dynamic experiments had a period of 2 min with a 50% duty cycle (1 min on and 1 min off). Lines represent fits obtained using models described in Section 3.4.

ethylene undergoes secondary reactions at higher conversions to produce CO_x. Dynamic and SS selectivities in Figure 1 are essentially identical, suggesting minimal impact of separating oxidation and reduction half cycles on selectivity-conversion trends. Note that larger residence times are required in order to reach the same conversion under dynamic versus SS conditions. The lack of dynamic selectivity enhancement upon minimizing mixing between gas phase ethane and oxygen noted here mirror previous findings of the Bell and Iglesia groups[11] that reported identical selectivity-conversion data for staged and cofeed operation of ethane ODH over VO_x/Al_2O_3. The rates of all three reactions in Scheme 1 being independent of O_2 pressure were suggested as the basis for the negligible differences between selectivity for the staged and cofeed modes of operation.[11]

The lack of dynamic enhancement encouraged an investigation into the effect of O_2 concentration on rates over the VO_x/Al_2O_3 catalyst. An inspection of the intercepts of the selectivity-conversion plot provides information about the O_2 concentration rate dependence of the two parallel primary reactions (1 and 2 in Scheme 1). The rate of ethylene oxidation (i.e., r_3 for R3 in Scheme 1) can be considered negligible ($r_3 \ll r_1$ and r_2) in the limit of 0% ethane conversion due to the low C_2H_4/C_2H_6 ratios prevalent under these conditions.[24] C_2H_4 selectivities in Figure 1 for the 1 and 10% O_2 data overlap and share the same intercept. The insensitivity of the intercepts to changes in O_2 concentration suggests that C_2H_6 ODH and C_2H_6 combustion reactions (r1 and r2 in Scheme 1) have identical O_2 concentration dependencies. The nonzero CO_x selectivity intercept values negate the possibility that the intercepts are identical owing to the lack of parallel ethane combustion reactions; this contrasts with the results of Dinse et al., who found a selectivity intercept of 100% for ethane ODH over VO_x/Al_2O_3, albeit over a 10 wt % VO_x catalyst using 16% C_2H_6.[16] Moreover, ethane consumption rates and ethylene selectivities at 550 °C both are independent of O_2 pressure (Figure 2), suggesting that the rates of all three reactions in Scheme 1 are likely independent of O_2 pressure. Further examples of O_2 independent rates can be found in Section S9.

Our inference that ethane ODH reaction rates on supported vanadia catalysts are independent of O_2 concentration is in

https://doi.org/10.1021/acscatal.3c06066
ACS Catal. 2024, 14, 7877−7892

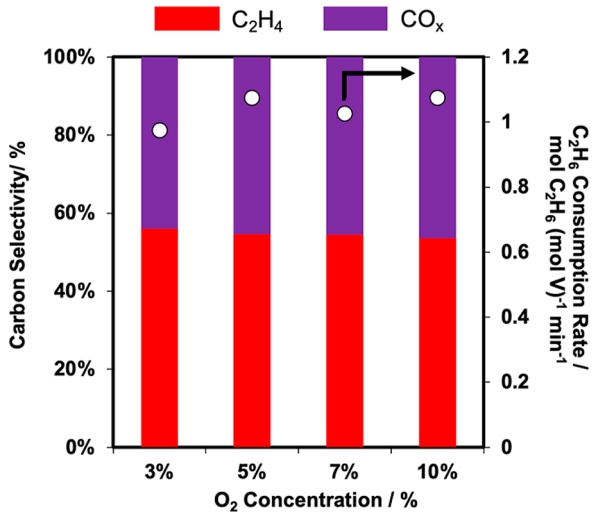

Figure 2. C_2H_4 and CO_x carbon selectivities [%] and C_2H_6 consumption rates per mol vanadium as a function of O_2 concentration [%] at 3 mg sccm^{-1}, 550 °C, 1% C_2H_6, for 0.7 ML VO_x/Al_2O_3.

agreement with previous reports on supported vanadia catalysts.[3,4,11] The lack of an O_2 partial pressure dependency for the reaction rates in Scheme 1 explains why the carbon selectivity is independent of O_2 pressure during concentration forcing, much like the staged reactor used by Waku et al.[11] This suggests that a catalyst may only exhibit a difference in selectivity between dynamic and SSO if a subset of the reactions within the operative reaction network have distinct apparent reaction orders.[11,21] Kinetic parameters associated with ethane ODH over the VO_x/Al_2O_3 catalyst discussed thus far will be analyzed in more detail in Sections 3.3 and 3.4. Next, we extend our investigation to the effects of concentration forcing on MoO_x/Al_2O_3 catalysts which, unlike their VO_x counterparts, exhibit unique selectivity trends during periodic operation.

3.2. Dynamic and SSO over MoO_x/Al_2O_3. MoO_x finds use in a variety of selective oxidation catalysts,[6,10,15,19,25] and has also received attention in the context of ethane ODH, albeit to a lesser extent than supported vanadia catalysts. Recently, Novotný et al. reported the use of chemical looping ethane ODH to achieve higher ethylene selectivities compared to SSO over submonolayer MoO_x/Al_2O_3 catalysts.[19] In the current study, we investigate MoO_x/Al_2O_3 catalysts of three separate weight loadings −2.4, 7, and 22 wt %, which equate to approximately 0.2, 0.5, and 1.6 monolayers, respectively, assuming an Mo density of 5.0 Mo/nm^2.[19] Dynamic and SS selectivity-conversion plots at 550 °C for the 0.2, 0.5, and 1.6 ML MoO_x catalysts are shown in Figure 3A−C, respectively. Plots containing all products—C_2H_4, CO, and CO_2, rather than just C_2H_4 and CO_x—can be found in Section S10 of the SI. Unlike the VO_x/Al_2O_3 catalyst discussed in Section 3.1, dynamic ethylene selectivities at any given conversion value are greater than steady state selectivities, with the gap between the two broadening with increasing O_2 concentration. More specifically, increasing the O_2 concentration from 1 to 10% reduces ethylene selectivity under both SSO and FDO, but does so to a greater extent for the former than the latter. The lower selectivity intercepts in Figure 3 at higher O_2 concentrations suggest a stronger O_2 concentration dependency of ethane combustion relative to ethane ODH (r_2 relative to r_1), and the more rapid decrease in selectivity with conversion indicate a stronger O_2 concentration dependency of ethylene combustion reactions relative to ethane ODH (r_3 relative to r_1). In addition, the catalyst temperature appears to have little influence on dynamic and SS selectivity values, as illustrated in Figures S9−S11 for a temperature of 590 °C over the 0.2 and 0.5 ML catalysts, aligning with similar observations by Novotný et al. for chemical looping ethane ODH over MoO_x/Al_2O_3 catalysts.[19]

To more directly probe the hypothesis that O_2 concentration disproportionately affects unselective combustion rates, SS ethane consumption rates and product selectivities at a specific residence time and reaction temperature are plotted in Figure 4 versus O_2 concentration. Additional plots are provided in Section S11. Ethane consumption rates increase slightly with O_2 pressure, suggesting that the primary reactions may have a very small O_2 dependency. Later sections will more discuss a more rigorous fitting of experimental data to determine reaction orders. Ethylene selectivity values, however, decrease monotonically with O_2 concentration, suggesting that the ethylene oxidation rate (r_3) increases with O_2 pressure.

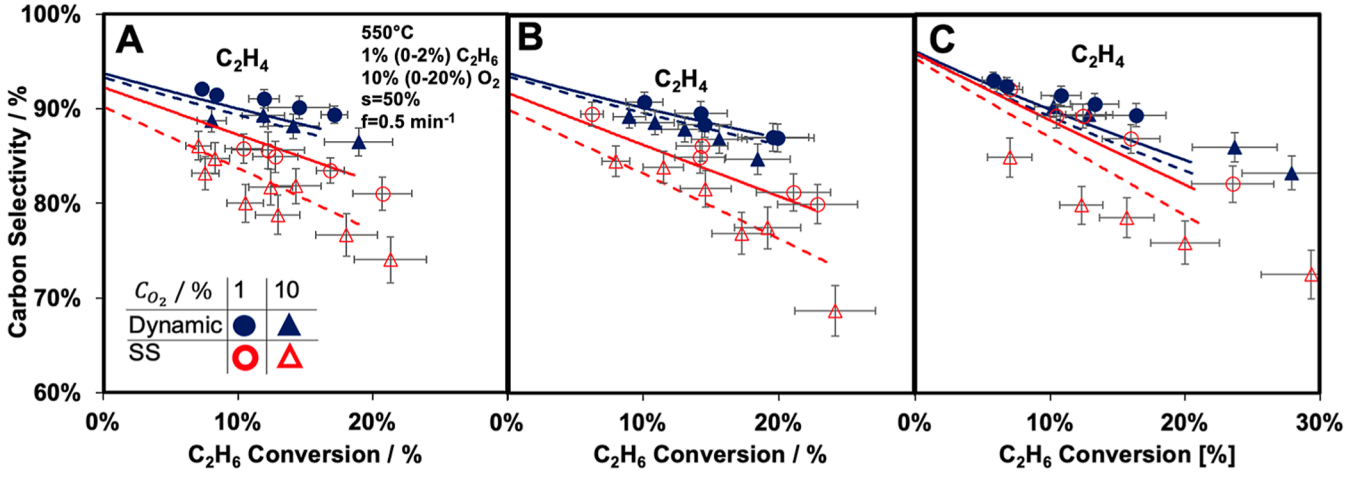

Figure 3. Dynamic and SS C_2H_4 carbon selectivities [%] as functions of C_2H_6 conversion [%] at 550 °C and 1 and 10% O_2 for 0.2 ML (A), 0.5 ML (B), and 1.6 ML (C) MoO_x/Al_2O_3 with 1% C_2H_6. Dynamic experiments had a period of 2 min and a 50% duty cycle. Lines through data indicate predictions obtained from models described in Section 3.4.

https://doi.org/10.1021/acscatal.3c06066
ACS Catal. 2024, 14, 7877−7892

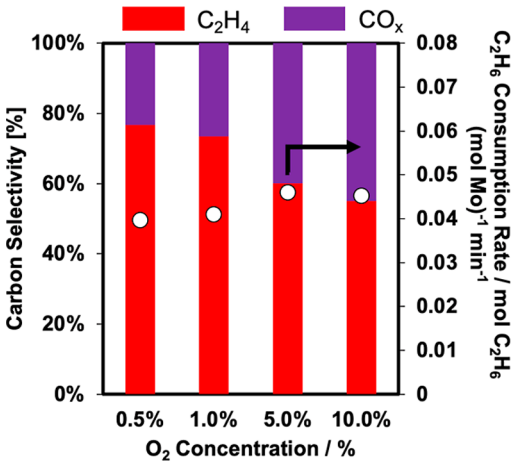

Figure 4. C_2H_4 and CO_x carbon selectivities [%] and C_2H_6 consumption rates per Mo as a function of O_2 concentration [%] at 8 mg sccm^{-1}, 590 °C and 1% C_2H_6 for 7 wt % MoO_x/Al_2O_3.

Trends for alumina supported vanadia and molybdena catalysts indicate that dynamic selectivity enhancement observed on the latter are a consequence of combustion reactions being characterized by higher O_2 reaction orders than the selective ODH reaction. Interestingly, these non-zero reaction orders satisfy analogous aforementioned criteria for enhancement in membrane reactors.[21]

Trends as a function of molybdena loading are critical to consider in light of findings of the Lamb group, wherein chemical looping-derived selectivity enhancement compared to the cofeed mode of operation was observed only for samples with submonolayer, not supramonolayer loadings.[19] The data in Figure 3 show that dynamic enhancement can in fact be achieved even at loadings that necessarily create multilayer molybdena domains as long as sufficiently high O_2 concentrations are employed. These observations point to the need for a more nuanced, quantitative evaluation of kinetic parameters as a function of MoO_x loading that provide non-qualitative insights into the effect of catalyst weight loading and reaction conditions on the extent of dynamic enhancement. In the following section, we investigate kinetic parameters corresponding to the three individual reactions in the triangular reaction network in Scheme 1 by fitting measured SS selectivity-conversion data to an integral power law kinetic reactor model.

3.3. Power Law Model Reaction Network Analysis for VO_x and MoO_x/Al_2O_3. Kinetic parameters for the 0.2, 0.5, and 1.6 ML MoO_x (2.4, 7, and 22 wt % MoO_x, respectively) and 0.7 ML VO_x (3 wt % VO_x) on Al_2O_3 catalysts were obtained by fitting SS data presented in previous sections to the reaction rates in Scheme 1 using the standard steady-state plug flow reactor (PFR) design equation and rate expressions as follows:

$$\frac{dC_i}{d\tau} = R_i \tag{3}$$

$$\tau = \frac{W}{F(T)}\left[\frac{\text{mg cat}}{\text{sccm}}\right]$$

$$r_1 = k_1'[C_2H_6][O_2]^a \tag{4}$$

$$r_2 = k_2'[C_2H_6][O_2]^b \tag{5}$$

$$r_3 = k_3'[C_2H_4][O_2]^c \tag{6}$$

All data in this study were found to be kinetically limited and free of heat and mass transport artifacts, permitting the use of eq 3 for parameter estimation. Further discussion and calculations are reported in Section S1 of the Supporting Information. Volumetric flow rates were calculated using the temperature of the gas measured just upstream of the catalyst bed,[27] and all of the SS data were fit using the integral as opposed to the differential model. Data fitting was conducted using the trust region reflective algorithm for bounded minimization of the objective function (eq 7)

$$\text{RSS} = \sum_{\text{experiment}}^{M}\sum_{\text{species}}^{N}\frac{(C_{\text{exp}} - C_{\text{model}})^2}{C_{\text{exp}}} \tag{7}$$

95% confidence intervals were determined from an approximation of the covariance matrix and the proper t-statistic parameter as detailed by van der Linde et al.[23] Further details on the fitting process including parity plots and confidence interval calculations can be found in Section S12.[23]

Estimated reaction orders in Table 1 show that all three reactions over the VO_x/Al_2O_3 catalyst are independent of O_2 concentration, aligning with the zeroth-order O_2 dependence for supported VO_x catalysts reported by Waku and Argyle.[3,4,11] Moreover, the lack of dynamic enhancement noted in our data mirror findings of Waku et al., who observed no discernible impact of staged feed operation on VO_x/Al_2O_3 catalysts because of the absence of O_2 concentration dependencies of reaction rates.[11] During bang−bang (on−off) modulation experiments used in our study, regions containing minimal (or no) gas phase O_2 and only gas phase reductant (i.e., ethane) are accessed alternatingly, analogous to membrane reactors which operate by distributing the desired O_2 molar flow rate over the length of the bed so as to create regions of minimal (or zero) O_2 concentration.

Table 1. Estimated Kinetic Parameters for 0.2, 0.5, and 1.6 ML MoO_x, and 0.7 ML VO_x on Al_2O_3 at 550 and 590 °C[a]

catalyst	T [°C]	k_1' (× 10^{-1})	k_2' (× 10^{-2})	k_3' (× 10^{-1})	a	b	c
3 VO_x	550	3.5 ± 0.3	7 ± 2	8 ± 4	0 ± 0.1	0.1 ± 0.3	0 ± 0.4
2 MoO_x	550	0.6 ± 0.02	0.7 ± 0.2	0.8 ± 0.3	0	0.18 ± 0.2	0.17 ± 0.3
	590	1.4	1.6 ± 0.1	1.5 ± 0.1	0 ± 0.2	0.37 ± 0.07	0.06 ± 0.07
7 MoO_x	550	0.79 ± 0.03	0.9 ± 0.1	0.8 ± 0.3	0	0 ± 0.1	0.29 ± 0.16
	590	1.8 ± 0.1	1.21 ± 0.05	2.3 ± 0.4	0	0 ± 0.4	0.26 ± 0.13
22 MoO_x	550	0.9 ± 0.06	0.7 ± 0.2	1.2 ± 0.3	0 ± 0.05	0.2 ± 0.3	0.3 ± 0.2

[a]Power law rate equations in Scheme 1 were used with eq 4 to obtain the parameters. Rate constants are reported in $(cm^3)^{1+i}$ mg_{cat}^{-1} min^{-1} μmol^i, where, i is the apparent reaction order of O_2 for reaction i (a, b and c in Table 1). Note: all values are reported with ±95% confidence intervals. All values missing confidence intervals had intervals less than 2 orders of magnitude of the reported value.

https://doi.org/10.1021/acscatal.3c06066
ACS Catal. 2024, 14, 7877−7892

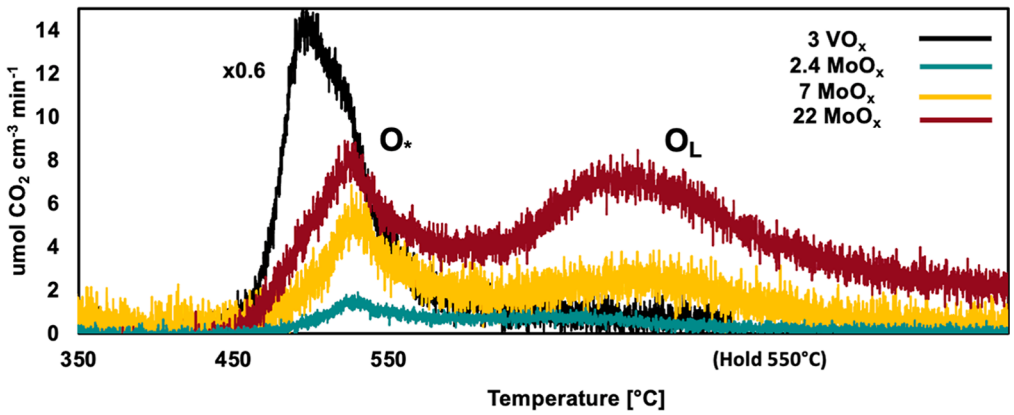

Figure 5. CO TPR of 0.2, 0.5, and 1.6 ML MoO_x and 0.7 ML VO_x on Al_2O_3 catalysts with 10 °C/min ramp rates. TPR curve for the 0.7 ML VO_x catalyst scaled by a factor of 0.6. The samples were held isothermally after reaching a temperature of 550 °C.

Table 2. Amount of Chemisorbed and Lattice Oxygen per mol Metal [mol M] and per cm^3 of Catalyst Estimated by CO TPR and BET Surface Areas and Estimated Crystallite Sizes of Catalysts for 0.2, 0.5, and 1.6 ML MoO_x and 0.7 ML VO_x Catalysts

catalyst	O concentration [mol O/mol M]	O concentration [μmol O/cm^3]	chemisorbed oxygen (O_*) [μmol O/cm^3]	lattice oxygen (O_L) [μmol O/cm^3]	O_*/O_L ratio	BET surface area [m^2/g cat]	crystallite size [nm]
0.2 MoO_x	0.56	50	30	20	1.5	63	29/11
0.5 MoO_x	0.38	98	49	49	1.0	50	31/30
1.6 MoO_x	0.31	250	100	150	0.67	55	63/35
0.7 VO_x	0.99	200	120	80	1.5	66	3

In contrast with VO_x catalysts, combustion pathways on MoO_x/Al_2O_3 catalysts at all three weight loadings and both reaction temperatures exhibit higher O_2 sensitivities compared to selective oxidation pathways (Table 1). Specifically, the ODH reaction rate (r_1) was found to be independent of O_2 concentration, unlike the combustion reactions (r_2 and r_3) that were found to be fractional positive-order in O_2. The lack of mixing between C_2H_6 and O_2 during FDO results in higher selectivities relative to SSO because the reaction of ethane exclusively in the absence of gas phase O_2 under dynamic operating conditions suppresses combustion reactions more so than the selective ODH reaction. This criterion is similar to that required for selectivity enhancement within membrane reactors, as described elsewhere ($a < b$ or c or more generally $n_{Sel.} < n_{Unsel.}$).[11,21] Much like membrane reactors, O_2 concentration dependencies of unselective relative to selective reactions serve as a criterion to deduce the viability of obtaining selectivity enhancement by employing non-steady state modes of operation.

Differences in apparent reaction orders with respect to O_2 are not solely responsible for the observed differences between dynamic and SS selectivity profiles. Another important feature of relevance is the magnitude of the unselective relative to the selective reaction rate. For example, the ratio of ethane ODH to ethane combustion rate constants at equivalent units ($k_1'/(k_2'[O_{2,ref}]^{b-a})$) for an intermediate O_2 concentration of 5% are at a minimum 5.0 and 8.0 for the VO_x and MoO_x catalysts, respectively, across 550 and 590 °C (Table S2, Supporting Information). On the other hand, ratios between ethane ODH and ethylene combustion ($k_1'/(k_3'[O_{2,ref}]^{c-a})$) at 550 °C are 0.4, 0.9, 1.3, and 1.0 for the 0.7 ML VO_x, 0.2, 0.5, and 1.6 ML MoO_x catalysts, respectively. At 590 °C, these ratios reach 1.0 for both the 0.2 and the 0.5 ML MoO_x catalysts. The $k_1'/(k_3'[O_{2,ref}]^{c-a}$ ratio of 0.4 observed over the VO_x catalyst is consistent with the higher reactivity of ethylene compared to ethane reported previously by Waku et al.[11] The increasing divergence between dynamic and SS selectivities at higher conversions therefore appear to be caused by differences in ethylene combustion rates. Unselective reactions must not only have larger apparent O_2 orders but also rate constants that are large enough to reasonably influence product selectivity. While the power law kinetic model is sufficient at describing SS data, it is limited in its ability to estimate features like accumulation, which are present during dynamic operation. The following section will investigate the use of a more detailed non-steady state kinetic model involving oxygen species stored on and within the catalytic material, and that participate in reactions with gaseous reductants.

3.4. Oxygen Speciation and the Basis for Fractional Order O_2 Dependencies. The greater disparity between MoO_x/Al_2O_3 SS and dynamic performance at higher O_2 concentrations (Figure 3) along with the decreasing ethylene selectivity with increasing O_2 concentration (Figure 4) can be rationalized using the higher O_2 concentration sensitivities listed in Table 1 for combustion reactions relative to the ODH reaction. We hypothesize that the greater O_2 concentration sensitivities of combustion reactions are a consequence of the involvement of multiple active oxygen species in catalytic turnovers. An extensive body of literature exists that discusses the potential roles of lattice and chemisorbed oxygen in catalytic partial oxidation reactions. Chemisorbed oxygen (O_*) is often proposed to be responsible for total oxidation of ethane to CO_x due to its electrophilic nature, while nucleophilic lattice oxygen (O_L) is linked to ethane partial oxidation to ethylene.[5,8,17,22] Such an inclination of chemisorbed oxygen toward favoring undesired combustion reactions would help explain the adverse effect of O_2 pressure on ethylene selectivity, i.e., the surface would be expected to

https://doi.org/10.1021/acscatal.3c06066
ACS Catal. 2024, 14, 7877−7892

first be populated by selective lattice oxygen at low O_2 pressures prior to forming chemisorbed species at higher pressures. Reoxidation cycles carried out at a higher O_2 concentration would therefore increase the cycle average ratio of unselective chemisorbed oxygen to lattice oxygen (O_*/O_L).

The amounts of reactive oxygen in the VO_x and MoO_x catalysts were probed using CO temperature-programmed reduction (TPR), with the molar flow rate of CO_2 per unit bed volume as a function of time plotted in Figure 5. The integrated areas under the TPR temporal curves represent the total amount of available oxygen per cc of catalyst, and are listed in Table 2. MoO_x samples exhibit two distinct reduction peaks—one centered at 500 °C and another at 550 °C. We propose that the oxygen released at lower temperatures is chemisorbed onto the catalyst surface (O_*), whereas oxygen released at higher temperatures originates from the MoO_x crystal lattice (O_L). Chemisorbed oxygen can only be formed on the surface, whereas lattice oxygens are present within both the surface and the subsurface of the metal oxide crystallites. It is likely that surface chemisorbed oxygens are reduced prior to the lattice oxygen during reduction with CO; hence, their peak designations at 500 and 550 °C, respectively. Furthermore, increases in crystallite radius are expected to lead to greater increases in the concentration of subsurface lattice oxygen relative to surface chemisorbed oxygen. This trend is indeed observed in Table 2, which shows that the O_*/O_L ratio decreases from 1.5 to 0.67 when increasing MO_x coverage (from 0.2 to 1.6) and crystallite size. Increasing molybdena loadings result in larger chemisorbed and lattice oxygen densities per unit bed volume (Table 2). The total oxygen content per mol Mo, on the other hand, decreases with increasing loading due to the propensity of MoO_x domains to form, at higher loadings, extended aggregates that contain "bulk" molybdenum in addition to surface molybdenum. These larger MoO_x aggregates formed at higher weight loadings reduce the fraction of accessible oxygen due to intracrystalline diffusional resistances, thereby decreasing the amount of available oxygen on a per mol metal basis.[28−30] Crystallite sizes calculated using the Scherrer equation increase with MoO_x weight loading due to the formation of larger domains at higher weight loadings (Table 2).[31−37] Table 2 also shows that the ratio of lattice to chemisorbed oxygen extracted with CO increases with weight loading, presumably because extended MoO_x crystal lattices lend stability to the surface that in turn makes O_2 chemisorption on higher weight loading samples less energetically favorable than on low weight loading samples.

Lattice to chemisorbed oxygen ratios could also increase with weight loading simply because of lower surface to volume ratios because chemisorbed oxygen, unlike lattice oxygen, originates exclusively from the surface of the crystallites. The fact that the sample with the highest weight loading (1.6 ML MoO_x) appears to not be fully reduced and exhibits a protracted tail that is likely a result of constrained oxygen diffusion in the larger MoO_x crystallites lends credence to this hypothesis.[22,28−30,34] As more oxygen is stripped from the surface of the MoO_x crystallites, subsurface oxygen must diffuse from the bulk of the crystallite to the surface to participate in the reaction, with the time scale for oxygen diffusion scaling with the square of crystallite size. The impact of oxygen diffusion within metal oxide crystallites on the catalytic performance of oxidation reactions has been considered by several other investigators.[22,30,38] The influence of intracrystalline oxygen diffusion on SS and dynamic kinetics will be discussed in Section 3.5.

Unlike MoO_x/Al_2O_3 catalysts that exhibit two distinct reduction peaks, the TPR profile for VO_x/Al_2O_3 contains a single peak at 490 °C with a less prominent shoulder at 500 °C that is barely distinguishable from the low-temperature reduction peak (Figure 5). Various other works report only a single H_2 TPR peak in the vicinity of 500 °C for supported VO_x,[33,35,39,40] but some identify a H_2 consumption peak with a shoulder on samples with lower VO_x loadings, akin to the peak shape observed in Figure 5.[35,39] We interpret the TPR shoulder to suggest the presence of lattice oxygens (O_L) that exhibit reducibilities that are not easily distinguishable from chemisorbed oxygen species that undergo reduction at slightly lower temperatures. The peaks were deconvoluted into two separate individual peaks and then integrated, with the low temperature peak assigned to chemisorbed oxygen (O_*) and the high temperature one assigned to lattice oxygen (O_L). MoO_x and VO_x catalysts are contrasting in that both types of oxygen species in VO_x/Al_2O_3 exhibit reducibilities that are barely distinguishable, unlike MoO_x/Al_2O_3 ones in which nearly all the chemisorbed oxygens are extracted prior to the reduction of lattice oxygens at higher temperatures. Overall, the TPR profiles in Figure 5 suggest that lattice oxygens in MoO_x catalysts are much more stable compared to chemisorbed oxygens, unlike the VO_x catalyst in which lattice oxygen species are only minimally more stable than the corresponding chemisorbed oxygen species. This dissimilar behavior of lattice and chemisorbed oxygen on the two classes of catalysts has significant bearing on the question as to why only one class of catalysts exhibits non-zero O_2 reaction orders and dynamic selectivity enhancement but not the other—an aspect explored more fully in the next section.

3.5. Two-Oxygen Kinetic Model. The power law kinetic model described in Section 3.3 for the reaction network depicted in Scheme 1 describes the effect of oxygen pressure on individual reaction rates at a semiempirical, global kinetic level. As mentioned earlier, such a model has limited capability in describing dynamic operation over oxide catalysts. In particular, such power law kinetic models cannot rigorously account for reactions utilizing oxygen stored within the catalytic material.[10,15−17,22] In this section, we develop a more detailed kinetic model that accounts for both halves of the MvK redox cycle—the reduction and oxidation half cycles—as well as the participation of lattice and chemisorbed oxygen in both desired ODH and undesired combustion reactions. Scheme 2 details data collection, fitting, and validation methods used for the power law and 2 oxygen site

Scheme 2. Methodology Used for Data Analysis and Fitting to Obtain Kinetic Parameters, Followed by the Validation of Obtained Parameters

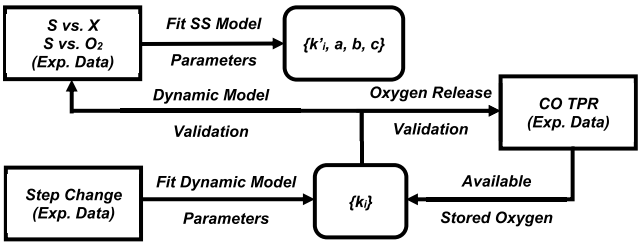

https://doi.org/10.1021/acscatal.3c06066
ACS Catal. 2024, 14, 7877−7892

models. Power law kinetic parameters were determined by fitting selectivity versus C_2H_6 conversion and O_2 concentration data sets. Step change experiments were used to estimate parameters in Scheme 3 for the two-oxygen model, while CO

Scheme 3. Reaction Pathways Used in Model with Chemisorbed (red) and Lattice (Blue) Oxygens over the MoO_x Catalyst, VO_x by Inference

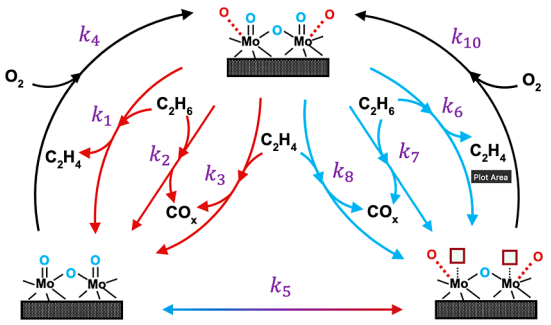

TPR data were used to determine the amount of available oxygen in the catalyst. Selectivity versus conversion plots estimated using the model are validated by comparing them to experimental data in the previous section at different oxygen concentrations. Finally, O_* and O_L release profiles estimated by the model during step change experiments are qualitatively compared to peak locations in the CO TPR data. Further details on the parameter estimation procedure used are included in Sections S12 and S13 of the Supporting Information.

The existence of chemisorbed and lattice oxygen species on the oxide catalyst surface (MoO_x or VO_x) and the identification of multiple reduction peaks during CO TPR leads to consideration of the two-oxygen model depicted in Scheme 3. The scheme considers ODH and combustion routes involving either chemisorbed (O_*) or lattice (O_L) oxygen—steps 1−3 and 6−8, respectively. Each of these steps creates either a chemisorbed or lattice oxygen vacancy resulting from carbon−oxygen bond formation or hydroxyl recombinative desorption steps. Reoxidation of chemisorbed and lattice oxygens are accounted for in O_2 adsorption steps 4 and 10, along with interconversion between the two types of oxygen (step 5).[42,43] Rate expressions for each of the 10 steps considered in the model are listed in Table 3, along with the corresponding rate constant values obtained from regressing against step change kinetic data.

Under SS catalytic conditions, the rates of all steps in Scheme 3 including reduction and oxidation half cycle steps must be considered in describing the experimentally measured data. This means that 10 kinetic parameters would need to be simultaneously estimated from a fit of the SS data. We used an alternative approach to estimate kinetic parameters that involved regressing separately the reduction and oxidation half cycle data measured after subjecting the catalyst to step changes in reductant and oxidant concentration as part of the dynamic experiments. This approach allowed us to reduce the number of kinetic parameters estimated during each stage of the model regression process. Step change experiments were conducted by flowing ethane over the bed for 1 min after the catalyst was fully oxidized, then exposing the bed to an N_2 purge for a minute, followed by oxidation with O_2 for 1 min. Ethylene and CO_x concentrations remained below detection levels during the oxidation step, confirming a lack of significant residual carbon and the occurrence, exclusively, of reoxidation steps only during this half cycle. Oxidation steps are affected only by oxygen adsorption (steps 4 and 9) and migration (step 5) rate constants; reduction steps, on the other hand, are affected by all other rate constants in the reaction scheme considered except steps 4 and 9.

Much like the SS power law fit in the previous section, rates during non-steady state operation were confirmed to be unaffected by mass and heat transfer limitations, permitting use of the following time-dependent equations for non-steady state operation also used by Huang et al., who modeled the transient conversion of butane to maleic anhydride.[22] The following transient pseudohomogeneous reactor (TPHR) model was used to analyze the step change data:

Bulk phase balances

$$\varepsilon_{bed}\frac{dC_i}{dt} = -F(T)\rho_{cat}\frac{dC_i}{dW} + \rho_{cat}R_i \tag{8}$$

Surface balances

Table 3. Reaction Rate Equations and Estimated Rate Constants (k_i) Used in the Two-Oxygen Model in Scheme 3 Estimated from eqs 8−20[a]

reaction	rate expression $\left[\frac{\mu mol}{mg\text{-}cat \times min}\right]$	0.7 VO_x	0.2 MoO_x	0.5 MoO_x	1.6 MoO_x
		Chemisorbed (O_*)			
$C_2H_6 + O_* \rightarrow C_2H_4 + H_2O$	k_1 $[C_2H_6][O_*]$	3.1×10^{-20}	6.3×10^{-10}	3.5×10^{-14}	2.51×10^{-5}
$C_2H_6 + 5O_* \rightarrow 2CO_x + 3H_2O$	k_2 $[C_2H_6][O_*]$	1.1×10^{-17}	2.06×10^{-4}	2.31×10^{-4}	4.30×10^{-5}
$C_2H_4 + 4O_* \rightarrow 2CO_x + 2H_2O$	k_3 $[C_2H_6][O_*]$	7.00×10^{-3}	3.00×10^{-3}	3.49×10^{-3}	1.74×10^{-3}
$O_2 + 2* \rightarrow 2O_*$	k_4 $[O_2][*]^2$	6.35×10^{-3}	3.20×10^{-4}	3.30×10^{-4}	1.02×10^{-4}
$O_* + L \rightarrow * + O_L$	k_5 $[O_*][L]$	5.00×10^{-5}	5.00×10^{-4}	1.51×10^{-4}	1.56×10^{-5}
		Lattice(O_L)			
$C_2H_6 + O_L \rightarrow C_2H_4 + H_2O$	k_6 $[C_2H_6][O_L]$	6.56×10^{-3}	2.74×10^{-3}	2.10×10^{-3}	6.91×10^{-4}
$C_2H_6 + 5O_L \rightarrow 2CO_x + 3H_2O$	k_7 $[C_2H_7][O_L]$	9.00×10^{-4}	1.3×10^{-12}	1.1×10^{-14}	8.3×10^{-22}
$C_2H_4 + 4O_L \rightarrow 2CO_x + 2H_2O$	k_8 $[C_2H_6][O_L]$	9.3×10^{-20}	3.65×10^{-7}	1.72×10^{-10}	1.2×10^{-19}
$O_2 + 2L \rightarrow 2O_L$	k_9 $[O_2][L]^2$	4.48×10^{-9}	2.23×10^{-8}	1.56×10^{-9}	1.1×10^{-10}
$O_L + * \rightarrow L + O_*$	k_{-5} $[O_L][*]$	7.9×10^{-20}	4.7×10^{-13}	4.57×10^{-20}	1.0×10^{-10}

[a]Rate constants are reported in $cm^{3\times i}$ mg_{cat}^{-1} min^{-1} μmol^{i-1}, where, i is 2 and 3 for bimolecular and trimolecular reactions, respectively.

https://doi.org/10.1021/acscatal.3c06066
ACS Catal. 2024, 14, 7877−7892

$$C_{i,\mathrm{Tot}}\frac{\mathrm{d}\theta_{\mathrm{O},i}}{\mathrm{d}t} = \rho_{\mathrm{cat}}R_i \tag{9}$$

Boundary conditions:
Reduction

$$C_{\mathrm{C_2H_6}}(t, W=0) = \frac{a_{0,\mathrm{red}}}{1+\exp(-a_{1,\mathrm{red}}\times(t-a_{2,\mathrm{red}}))} \tag{10}$$

$$C_{\mathrm{C_2H_4}}(t, W=0) = C_{\mathrm{CO_x}}(t, W=0) = 0 \tag{11}$$

$$\theta_{\mathrm{O},*}(t, W=0) = \theta_{\mathrm{O,L}}(t, W=0) = 1 \tag{12}$$

Oxidation

$$C_{\mathrm{O_2}}(t, W=0) = \frac{a_{0,\mathrm{ox}}}{1+\exp(-a_{1,\mathrm{ox}}\times(t-a_{2,\mathrm{ox}}))} \tag{13}$$

$$\theta_{\mathrm{O},*}(t, W=0) = \theta_{\mathrm{O},*}(t=t_{\mathrm{f,red}}, W=0) \tag{14}$$

$$\theta_{\mathrm{O,L}}(t, W=0) = \theta_{\mathrm{O,L}}(t=t_{\mathrm{f,red}}, W=0) \tag{15}$$

Initial conditions:
Reduction

$$C_{\mathrm{C_2H_6}}(t=0, W) = C_{\mathrm{C_2H_4}}(t=0, W) = C_{\mathrm{CO_x}}(t=0, W) = 0 \tag{16}$$

$$\theta_{\mathrm{O},*}(t=0, W) = \theta_{\mathrm{O,L}}(t=0, W) = 1 \tag{17}$$

Oxidation

$$C_{\mathrm{O_2}}(t=t_{\mathrm{f,red}}, W) = 0 \tag{18}$$

$$\theta_{\mathrm{O},*}(t=0, W) = \theta_{\mathrm{O},*}(t=t_{\mathrm{f,red}}, W) \tag{19}$$

$$\theta_{\mathrm{O,L}}(t=0, W) = \theta_{\mathrm{O,L}}(t=t_{\mathrm{f,red}}, W) \tag{20}$$

The bulk phase species balance listed in eq 8 accounts for accumulation balanced by convection (first derivative with respect to catalyst weight) and reaction rate over the catalyst surface. It is notable that the volumetric flow rate denoted as F in eq 8 is a function of the bulk gas phase temperature. The concentration of stored oxygen is described by eq 9, where accumulation is balanced by its reaction rate. The concentrations of stored oxygen are normalized by their total concentration determined from CO-TPR experiments (Section S6 of the Supporting Information) and are listed in Table 2. The empirical parameters $a_{0,i}$, $a_{1,i}$, and $a_{2,i}$ (i = red, ox) describe the step inputs and were estimated using the following method. The setup for the step change experiment was designed to minimize effects that would complicate data analysis. Identical bulk phase temperatures were measured at the inlet and outlet of the catalyst bed, indicating isothermal operation. A perfect discontinuity comprising an idealized discontinuous step function of concentration with time is difficult to achieve in practice due to axial dispersion. To take nonidealities into account, reduction and oxidation boundary conditions were determined by measuring step changes of C_2H_6 and O_2 in the bypass of the reactor and used to fit parameters $a_{0,i}$, $a_{1,i}$, and $a_{2,i}$ in the sigmoid functions, eqs 10 and 13. Further details of the fitting can be found in Section S13. Previous work demonstrated that the spread of a step change function in the presence of axial dispersion can be approximated with a Peclet number analysis.[40] The resulting spread of the step change for ethane and oxygen were estimated to be approximately 0.06 s for the temperature, flow rate, and reactor geometry used. The estimated spread was then incorporated into the parameter $a_{1,i}$ in eqs 10 and 13 to adjust the step change profile. Further details of the analysis can be found in Section S13. Saturation of both chemisorbed and lattice oxygens (i.e., fractional coverages of unity) was assumed at the onset of the reduction step—an assumption validated by the absence of an O_2 uptake rate a minute into the oxidation step. Initial and boundary conditions of the surface balances during the reoxidation step were estimated by solving eq 8 and using the surface coverage profiles at the end of the reduction step ($t = t_{\mathrm{red}}$).

Estimated parameters from the reduction and oxidation step change experiments for Scheme 3 reactions are listed in Table 3, with further details provided in Section S12. The relative magnitudes of parameter estimates indicate that reoxidation of both the VO_x and MoO_x catalysts occur by the sequential adsorption of O_2 onto surface vacancies followed by the irreversible filling of lattice vacancies. These reoxidation steps were also considered in other multioxygen models detailing adsorption and oxygen transfer on metal oxide catalysts.[17,22] The fit does not rule out other mechanisms but, as we show below, the model is consistent with the collective experimental findings reported here. Note in the discussion below that kinetic parameters of significance for the 1.6 ML MoO_x catalyst are distinct from those for the 0.2 and 0.5 ML catalysts, presumably due to the existence of oxygen diffusion artifacts in the former but not the latter (Section S14, Supporting Information).

The kinetic parameter estimates point to some similarities, and a few subtle differences between the MoO_x and VO_x catalysts considered. On both types of catalysts, lattice oxygen has a much greater propensity to effect the selective ODH reaction compared to chemisorbed oxygen. The roles of these two types of oxygens, however, are more nuanced when it comes to undesired combustion reactions. Over MoO_x catalysts, both routes for CO_x formation—the primary combustion of ethane as well as the secondary combustion of ethylene—preferentially involve chemisorbed oxygen. Chemisorbed oxygen on the 0.7 ML VO_x catalyst, on the other hand, simply affects secondary combustion of ethylene but not the combustion of ethane, which instead occurs over lattice oxygen. Oxygen speciation, therefore, appears to affect the triangular reaction network in Scheme 1 in a contrasting manner for the two catalysts considered. Whereas in the case of MoO_x, the nature of the active oxygen involved—lattice or chemisorbed—determines the identity of the species formed, i.e., ethylene or CO_x, in the case of VO_x/Al_2O_3, it determines the identity of the hydrocarbon converted, i.e., ethane or ethylene.

Both sets of conclusions are consistent with observations and suggestions from the prior literature. Chemisorbed oxygens that are not fully bound within an oxide lattice are considered as electrophilic, while lattice oxygen coordinated to multiple metal atoms are considered nucleophilic.[17−22] The electrophilic nature of chemisorbed oxygen has been proposed to promote scission of electron dense C−C and C═C bonds in ethane and ethylene, respectively, resulting in CO_x formation.[5,8,13,15,17,22,42,43] Conversely, nucleophilic lattice cleaves C−H bonds while preserving C−C bonds, resulting exclusively in the formation of ethylene, not CO_x.[5,8,13,15,17,22,42,43] Furthermore, the contrasting behavior

https://doi.org/10.1021/acscatal.3c06066
ACS Catal. 2024, 14, 7877−7892

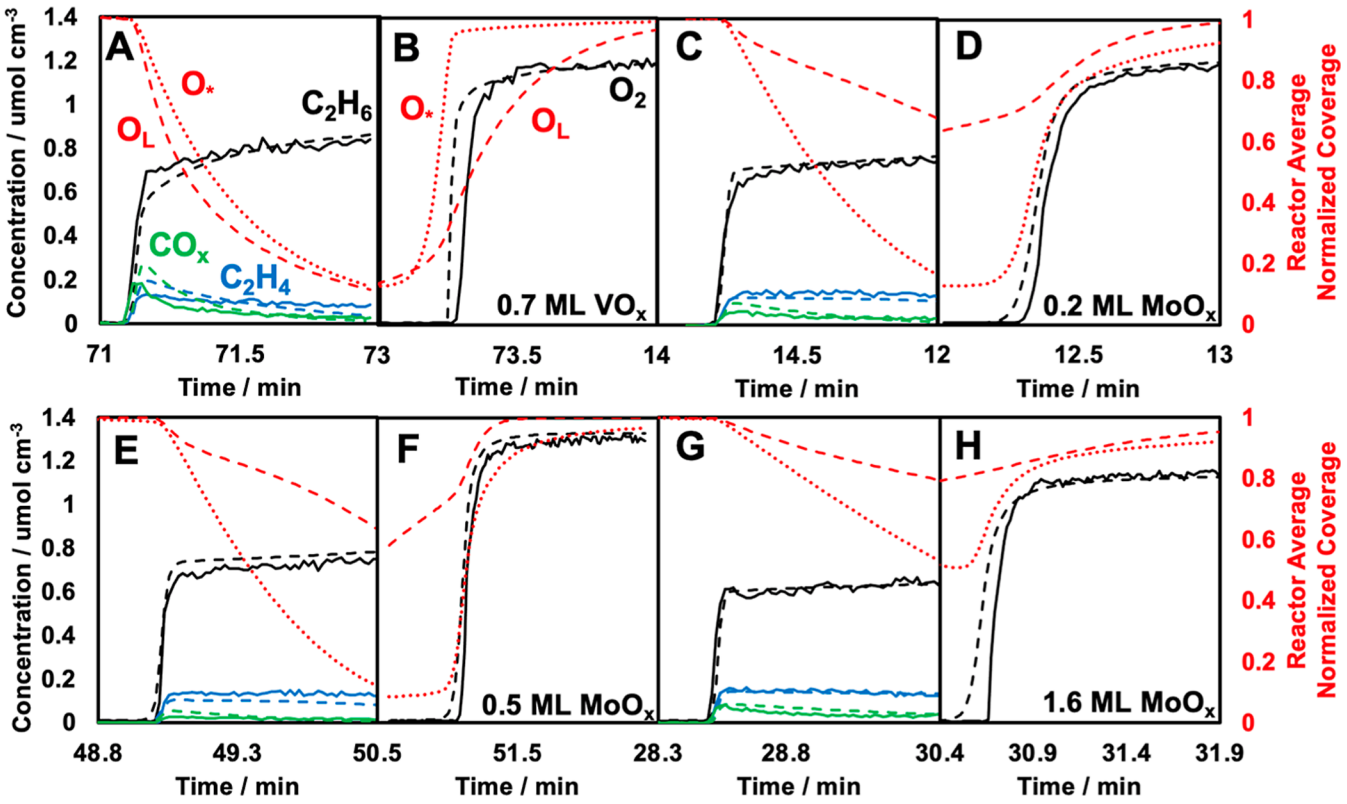

Figure 6. Step change reduction and reoxidation experiments for 0.7 ML VO_x (A,B), 0.2 (C,D), 0.5 (E,F), and 1.6 (G,H) ML MoO_x with 400 mg of catalyst at 550 °C, 50 sccm, 1 and 1% cyclic averages of C_2H_6 and O_2, respectively. For reactant and product concentrations, solid lines represent experimental data and the dashed lines represent model predictions, and for the oxygen coverages, solid and dashed lines denote chemisorbed (O_*) and lattice (O_L) coverages.

of VO_x/Al_2O_3 also follows an existing precedent in the open literature. Dinse et al. showed that rate constants associated with primary ethane ODH and combustion reactions over VO_x/Al_2O_3 were unaffected by a 50% prereduction of the catalyst, whereas secondary ethylene combustion rate constants decreased significantly upon prereduction.[16] The investigators attributed the lower rates of ethylene combustion over prereduced surfaces to its weaker binding onto vanadium sites carrying lower oxidation states.[16] Our work suggests that lower ethylene combustion rates post reduction may also be a result of the depletion of chemisorbed oxygen species that contribute disproportionately to ethylene combustion relative to lattice oxygen in VO_x catalysts that our kinetic analysis suggests participate exclusively in primary ethane ODH and combustion reactions. The participation of different types of oxygen species in ethane ODH and ethane combustion reactions over MoO_x/Al_2O_3 but not VO_x/Al_2O_3 provides an explanation as to why the mode of reactor operation (dynamic or SS) and O_2 concentration affect selectivity in the limit of zero conversion for molybdena catalysts uninfluenced by bulk oxygen diffusion time scales (Figure 3A,B) but not the 0.7 ML vanadia catalyst (Figure 1). We presume that these differences in the roles of lattice and chemisorbed oxygen are a consequence of the fact that chemisorbed oxygens on MoO_x catalysts are much more reducible and reactive compared to the corresponding lattice oxygens, unlike VO_x/Al_2O_3, on which both types of oxygen have similar reducibilities.

Figure 6A–H shows the experimentally measured and model predicted concentration temporal profiles as solid and dashed lines, respectively, as well as the reactor (length)-averaged chemisorbed and lattice oxygen contents normalized by the values available at the start of the reduction step. A notable feature during the reduction of the MoO_x catalysts depicted in Figure 6C,E,G is the maxima in CO_x concentration, unlike the ethylene concentration profiles that increase monotonically with time. As described earlier, our model suggests that both primary and secondary combustion reactions on MoO_x catalysts occur over chemisorbed oxygen, resulting in a rapid decrease in reactor O_* content. The CO_x formation rate may therefore go through a maxima, unlike ethylene formation rates that increase monotonically due to the lower stoichiometric oxygen requirement combined with the replenishment of lattice oxygen species (from chemisorbed oxygen) detailed in Scheme 3 and Table 3.

The trends in the reactor–average profiles of chemisorbed (solid) and lattice (dashed) oxygen species in Figure 6A–H provide insights into the transient performance on both catalysts. Figure 6A shows that both chemisorbed and lattice oxygen coverages decrease similarly with time during the reduction cycle over VO_x/Al_2O_3. The near-simultaneous depletion of chemisorbed and lattice oxygen aligns with reducibilities for the two oxygen species that are nearly indistinguishable in the CO TPR data (Figure 5). The similar reducibilities for the two oxygen species on VO_x catalysts are also consistent with TPR profiles reported previously in the literature.[33,35,39,40] In contrast, reduction cycles for MoO_x catalysts in Figure 6C,E,G show rapid depletion of chemisorbed oxygen and a slower depletion of lattice oxygen, likely due to the significantly higher reducibility of chemisorbed oxygen relative to lattice oxygen on these

https://doi.org/10.1021/acscatal.3c06066
ACS Catal. 2024, 14, 7877–7892

samples. This trend can be further understood by examining the estimated parameters listed in Table 3. Specifically, rate constants for chemisorbed to lattice oxygen interconversion are larger for MoO_x samples than for the VO_x sample. Rapid mobility of oxygen from a chemisorbed state to a lattice position would result in higher fractional coverages of selective lattice oxygen during reduction half cycles in the MoO_x samples relative to VO_x samples, as shown in Figure 6A−H. This faster oxygen interconversion results in O_*/O_L ratios less than unity on MoO_x catalysts, unlike the VO_x/Al_2O_3 catalyst, on which the O_*/O_L ratio remains closer to one.

The differences in oxygen interconversion rates are also reflected in oxidation cycle profiles. Reoxidation profiles of the VO_x catalyst in Figure 6B indicate that chemisorbed oxygen is replenished more rapidly than lattice oxygen, consistent with the estimated rate constant for oxygen adsorption onto VO_x/Al_2O_3 being larger than that for its migration from a chemisorbed state to the lattice (Table 3). Interestingly, the opposite oxygen coverage trends are observed for the MoO_x catalyst in Figure 6D,F,H, which show that lattice oxygen is replenished more rapidly than chemisorbed oxygen regardless of MoO_x loading. The much higher rates of oxygen interconversion relative to oxygen chemisorption on molybdena catalysts reflect the relative stability of MoO_x lattice oxygens compared to chemisorbed oxygens, detected in the form of separated CO TPR peaks for these two oxygen species. Both sets of experiments—CO TPR and step change data—suggest a greater energetic penalty associated with forming lattice oxygen vacancies on MoO_x catalysts. The reluctance to form lattice oxygen vacancies results in a facile conversion of chemisorbed oxygen to lattice oxygen, unlike the VO_x catalyst that lacks such a strong preference for the oxygen to exist within the crystal lattice rather than in a chemisorbed form on the surface.

Consistent with these findings, the TPHR model containing the Scheme 3 kinetics has been shown to qualitatively agree with our CO TPR experiments. Further model validation was carried out by comparing model predictions for selectivity-conversion data described earlier in Sections 3.1 and 3.2. Parameters and equations in Table 3 were applied in eqs 8 and 9 to simulate dynamic and SSO of VO_x and MoO_x/Al_2O_3 catalysts. The boundary condition at the reactor inlet was assumed to be a smoothed square wave during FDO, and a constant value during SSO. Ethylene selectivity as a function of conversion was obtained by adjusting catalyst bed length at the same flow rate. Model predictions of selectivities as functions of conversion for VO_x and MoO_x catalysts at 550 °C appear as lines in Figures 1 and 3 and successfully capture selectivity versus conversion trends. The model also captures both the negligible effect of FDO on VO_x/Al_2O_3 selectivity at 1 and 10% O_2 feed concentration (Figure 1), as well as the extent of the difference between dynamic and SSO that grows with O_2 concentration for the 0.2 and 0.5 ML MoO_x catalysts. The model, however, overestimates SS ethylene selectivity as a function of ethane conversion for the 1.6 ML MoO_x catalyst (Figure 3C), possibly due to the relevance of oxygen diffusion from the MoO_x bulk to the surface.

Effects of oxygen diffusion from the bulk of the metal oxide crystallite to the surface during the reduction step were therefore also considered in analyzing FDO data. Many groups have previously noted that intracrystalline bulk to surface oxygen diffusion rates that are insufficiently fast relative to oxygen consumption at the surface can affect estimated kinetic parameter values.[22,28−30,38,41] Time scales of bulk oxygen diffusion within the metal oxide crystallite were compared to the time scales of reaction occurring on the crystallite surface by recasting Weisz−Prater criteria (Section S14 of the Supporting Information). Intracrystalline oxygen diffusion limitations were found to be negligible for the 0.7 ML VO_x as well as the 0.2 and 0.5 ML MoO_x catalysts,[29,41] but not the 1.6 ML MoO_x catalyst. These calculations are consistent with the fact that the 1.6 ML catalyst is the only one of the four samples tested that carries a protracted tail in the TPR profile (Figure 5), aligning with observations in the prior literature of bulk oxygen diffusion-induced tails in TPR experiments.[30] Bulk oxygen diffusion limitations are likely attributable to the nearly 2-fold larger average crystallite sizes for the 1.6 ML catalyst compared to the 0.2 and 0.5 ML MoO_x catalysts inferred from powder XRD data (Table 2). The fact that the only material in our dataset that the model does not capture the dynamic and SS behavior of also happens to be the one that our calculations indicate are limited by bulk-surface oxygen diffusion time scales comparable to those of catalytic turnovers (Section S14) suggests to us that the lack of a model fit in this case may be a consequence of neglecting intracrystalline oxygen diffusion. The Silveston group, for example, showed that an accurate fitting of butane oxidation step change reduction profiles over VPO catalysts required consideration of intracrystalline oxygen diffusion rates.[22] Likewise, Redlingshöfer et al. demonstrated that slower rates of intracrystalline oxygen diffusion at lower temperatures can alter the rate limiting step of the MvK cycle, leading to differences in dynamic performance.[38] Analogous to these prior literature reports, our results suggest that quantitative agreement between model predictions and experimental data on higher loading samples may require accounting for the rates of oxygen diffusion to the surface. Having obtained quantitative agreement with the experimental data for all but the MoO_x catalyst carrying the highest weight loading, we now discuss the basis for the dynamic enhancement reported in Section 3.2 as inferred from the developed kinetic model.

3.6. Chemisorbed to Lattice Oxygen (O_*/O_L) Ratios, and the Basis for Dynamic Enhancement. In Sections 3.1, 3.2, and 3.3, we demonstrated that whereas all three reactions are O_2 concentration independent over the 0.7 ML VO_x catalyst, combustion and ODH reactions over MoO_x catalysts are, respectively, dependent and independent of O_2 concentration. ODH reactions over metal oxide catalysts have been proposed to proceed through an MvK mechanism comprising oxidation and reduction half cycle steps,[3,4,11,26] and facile reoxidation steps that are much faster relative to reduction half cycle steps suggested to result in an apparent zeroth-order O_2 dependence.[38] Note that we consider dissociative oxygen adsorption, as opposed to molecular adsorption that is assumed in the derivation of the MvK rate expression. Despite this difference, it can be shown that the dissociative adsorption model used here can successfully predict apparent reaction orders discussed in previous sections (Section S15). Specifically, the two-oxygen model predicts zeroth order behavior in O_2 when reoxidation rates are much faster than reduction rates. We plot in Figure 7 the ratio of the rate constant for reoxidation of chemisorbed oxygen vacancies (k_3) to the rate constant for reduction of chemisorbed oxygen by ethylene (k_4) adjusted by the total concentration of chemisorbed oxygens ($C_{*,Tot}$) using estimated parameters listed in Table 3. The ratio of the rate constants is multiplied by the total concentration of

https://doi.org/10.1021/acscatal.3c06066
ACS Catal. 2024, 14, 7877−7892

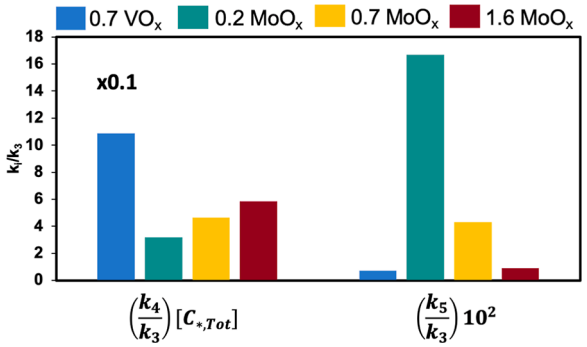

Figure 7. Ratios of rate constants for oxidation and oxygen transition to the rate constant of chemisorbed oxygen reduction by C_2H_4. For reference, rates are listed in Table 3. Ratios k_5/k_3 are multiplied by 100 to make them more visible on the *y*-axis scale chosen.

chemisorbed oxygens to keep the ratio dimensionless. VO_x/Al_2O_3 exhibits orders of magnitude higher k_4/k_3 $[C_{*,Tot}]$ ratios than MoO_x/Al_2O_3 catalysts, suggesting that the lack of an O_2 dependence of ethylene oxidation rate on the former are a consequence of oxidation half cycles that are much faster than reduction half cycles. Slower relative rates of oxidation half cycles relative to reduction half cycles on MoO_x samples, on the other hand, are consistent with nonzero, fractional orders in O_2. However, these ratios still do not explain why only combustion rates, but not ODH rates, are O_2 pressure dependent on the MoO_x catalysts, which can instead be explained by the ratio of the rate of chemisorbed oxygen migration to a lattice position (k_5) to its reduction by ethylene (k_3). The ratio k_5/k_3, plotted in Figure 7, is much smaller on the VO_x sample than on the MoO_x ones, indicating that chemisorbed oxygen on VO_x/Al_2O_3, once adsorbed, has a higher propensity to react with ethylene to form CO_x relative to its tendency to refill lattice vacancies through oxygen migration. Chemisorbed oxygens on MoO_x catalysts, on the other hand, have a higher propensity to migrate to refill lattice positions relative to their reduction by ethylene, resulting in a preferential replenishment of lattice oxygen relative to chemisorbed oxygen noted in Figure 6. As lattice oxygen participates solely in the ethane ODH reaction on MoO_x catalysts, rapid reoxidation would result in an apparent zeroth order in O_2. In short, the concentration of chemisorbed oxygen on MoO_x catalysts is suppressed by two separate factors that are captured by the data in Figure 7—slow reoxidation of chemisorbed oxygen vacancies, as well as the rapid migration from a chemisorbed state to a lattice position, resulting in a higher sensitivity to O_2 of rates catalyzed by chemisorbed oxygen species.

Estimated kinetic parameters listed in Table 3 and plotted in Figure 7 can also be used to understand a key observation made by the Lamb group that catalysts with greater than monolayer coverages of MoO_x, unlike those with submonolayer coverages, exhibit no dynamic enhancement.[19] This seemingly minor observation can be rationalized by analyzing the rate constant ratios as a function of MoO_x weight loading plotted in Figure 7. The reoxidation to reduction (k_4/k_3 $[C_{*,Tot}]$) and oxygen migration to reduction (k_5/k_3) rate constant ratios increase and decrease, respectively, with increasing MoO_x weight loading, with both ratios converging, at higher weight loadings, toward values estimated over the VO_x sample. The convergence of these ratios provides a kinetic

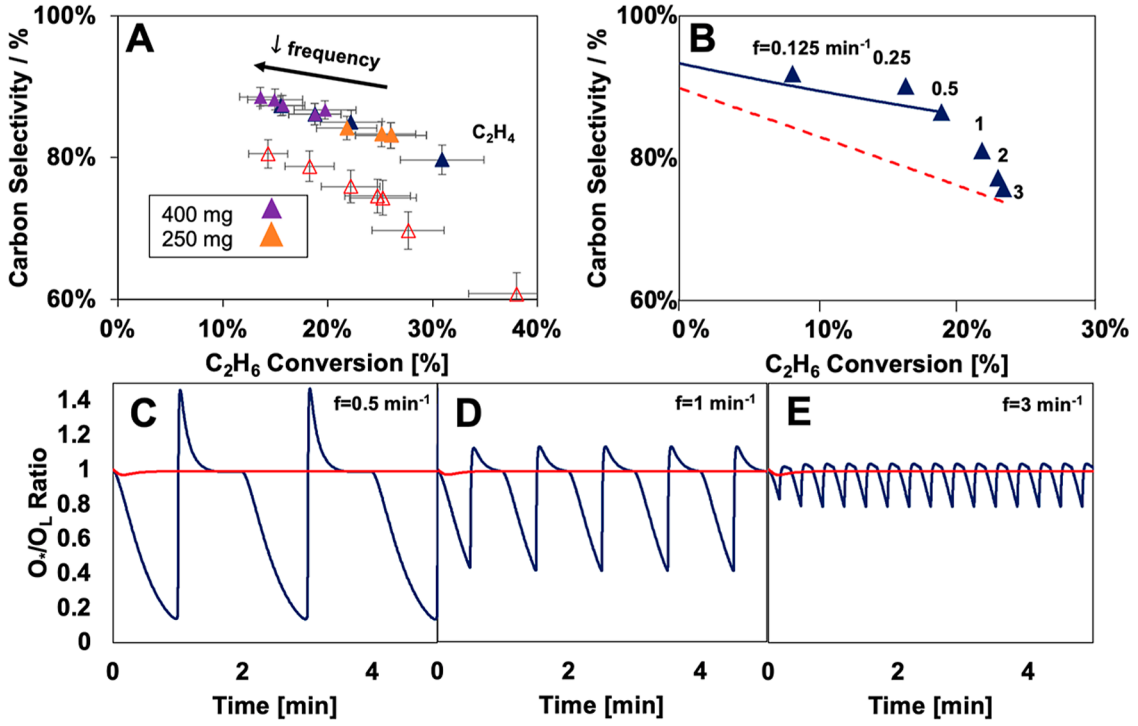

Figure 8. Carbon selectivity [%] vs C_2H_6 conversion [%] during dynamic operation by varying residence time (blue) and frequency of oscillations for 250 (orange) and 400 mg (purple) of 0.5 ML MoO_x catalyst at 50 sccm using 1% C_2H_6 and 10% O_2 at 590 °C (A). C_2H_4 carbon selectivity as a function of C_2H_6 conversion at 550 °C using 1% C_2H_6 and 10% O_2 at different frequencies estimated by the 2-oxygen model (triangles) compared to the experimental curves during FDO (blue line) and SSO (red dashed line) acquired by changing residence time (B). Reactor averaged O_*/O_L ratios as functions of time at frequencies of 0.5 (C), 1 (D), and 3 min^{-1} (E).

https://doi.org/10.1021/acscatal.3c06066
ACS Catal. 2024, 14, 7877−7892

interpretation for the mirroring in dynamic enhancement observed; just like the ratios on multilayer MoO_x catalysts begin to resemble those on the VO_x sample, the extent of dynamic enhancement can also diminish to the point where SS and dynamic selectivities overlap, akin to the VO_x catalyst that exhibits no dynamic enhancement. Specifically, on higher weight loading MoO_x catalysts, chemisorbed oxygens both reoxidize at a higher rate relative to being reduced (k_4/k_3 $[C_{*,Tot}]$)), and migrate to lattice oxygen at a lower rate relative to being reduced (k_5/k_3). These two factors are clearly detrimental to dynamic enhancement because higher reoxidation/reduction rate ratios result in a decrease in O_2 concentration dependency, and lower migration/reduction rate ratios limit the tendency of dynamic enhancement to suppress O_*/O_L ratios relative to those prevalent under SS conditions.

These kinetic factors are not the only ones, however, that can explain the detection of dynamic enhancement at low, but not high oxide weight loadings. Dynamic enhancement can be absent merely as a consequence of the larger oxygen storage capacities of higher weight loadings catalysts, especially multilayer ones. In our study, for example, CO TPR experiments indicate that the 1.6 ML MoO_x catalyst has a much larger amount of chemisorbed oxygen (100 μmol/cm^3) compared to the 0.5 ML one (49 μmol/cm^3). Higher concentrations of (unselective) chemisorbed oxygen on the 1.6 ML catalyst would be able to sustain unselective reactions for longer periods of time than the 0.2 and 0.5 ML MoO_x samples. The multilayer MoO_x catalysts would therefore need either higher reductant concentrations or longer reduction periods compared to the submonolayer samples to completely deplete the bed of chemisorbed oxygen. The interpretation of dynamic enhancement presented here suggests that a heavy depletion of MoO_x unselective chemisorbed oxygen is a prerequisite for higher ethylene selectivities being achieved under dynamic operating conditions. This effect of total oxygen capacity is further reflected in the transient CO_x profiles in Figure 6; the CO_x formation rate over the multilayer catalyst in Figure 6G appears to be more steady with time than the corresponding profiles over the submonolayer coverage samples in Figure 6C,E. Fractional coverages of chemisorbed oxygen for the submonolayer samples in Figure 6C,E drop below 0.5, whereas O_* coverages remain above 0.6 for the multilayer catalyst in Figure 6G. In summary, dynamic enhancement may be contingent not only on kinetic features such as an O_2 concentration dependency but also on choosing operating parameters that allow for a rapid depletion of chemisorbed oxygens that limit ethylene selectivity by effecting undesired combustion reactions.

3.7. Tuning O_*/O_L Ratios by Varying Modulation Frequency and Residence Time. Figure 8A shows ethylene selectivity values as a function of ethane conversion over 0.5 ML MoO_x at 590 °C for two different bed sizes and several modulation frequencies. Ethane conversions decrease and ethylene selectivity values increase as the modulation frequency is increased from 3 to 0.125 min^{-1} for both the 250 and 400 mg catalyst beds. Interestingly, altering the modulation frequency changes the ethane conversion while preserving the selectivity-conversion trend obtained by varying residence time, suggesting that changes in modulation frequency mimic changes in reactor residence time.

Figure 8B compares model-predicted selectivity values at various ethane conversions and frequencies at 550 °C to the selectivity curves obtained in previous sections. At low frequencies, similar selectivity-conversion trends as those obtained by varying residence time (and discussed in previous sections) are obtained. At higher frequencies, however, the model predicts a divergence from these trends and a convergence toward the SS selectivity-conversion curve, consistent with previous observations pointing to the convergence between SS and dynamic performance during higher frequency periodic operation of chemical reactors.[44−50] Such convergence between dynamic and SS solutions has been suggested to be a result of the reactor system being unable to respond to rapid perturbations owing to the time scale of modulation being smaller than the time scale of the reactor.[45,48,50] These effects of modulation frequency on dynamic enhancement can be further understood through an analysis of the transient chemisorbed and lattice oxygen coverages.

Lower modulation frequencies result in reduction half cycles that persist for longer periods of time, thereby depleting larger quantities of stored oxygen. Our kinetic analysis points to the participation of two types of oxygen—chemisorbed and lattice oxygen—that are depleted at distinct rates by each of the three reduction half cycle steps. Model-predicted bed length average ratios of chemisorbed to lattice oxygen (O_*/O_L) as a function of time are plotted in Figure 8C−E for three separate modulation frequencies −0.5, 1.0, and 3.0 min^{-1}. An asymmetry in O_*/O_L ratios can be inferred from these plots in that at all three frequencies the O_*/O_L ratios during the reduction step decrease below the steady state value to an extent greater than the relative increase during the oxidation step. This asymmetry in O_*/O_L ratios appears to be one of the key reasons for the dynamic enhancement observed at a frequency of 0.5 min^{-1} and suggests that at lower frequencies, dynamic operation consumes a larger quantity of unselective chemisorbed oxygen (O_*) relative to selective lattice oxygen (O_L) during the reduction step. Predicted O_*/O_L ratios move closer to SS values as the frequency is increased to a value of 1 min^{-1} (Figure 8D) and is almost equal to the SS value at a frequency of 3 min^{-1} (Figure 8E). The convergence between SS and dynamic ethylene selectivities at these higher frequencies can therefore be viewed as a consequence of similar O_*/O_L ratios within these two modes of operation, and provides a lens for rationalizing the limited dynamic enhancement noted by the Lamb group at greater than monolayer molybdena coverages but not submonolayer coverages.[19] Catalysts with higher weight loadings require longer periods (i.e., lower frequencies) during FDO to achieve significantly lower O_*/O_L ratios and concomitant higher ethylene selectivities compared to SSO conditions than catalysts with lower weight loadings. During extended reduction half cycles (i.e., at lower frequencies), more active oxygen is stripped from the catalyst, resulting in lower conversions as the reduction half cycle progresses. This, coupled with the irreversible and favorable migration of O_* to O_L, results in the lower O_*/O_L ratios captured in Figure 8C that help explain the dynamic enhancement observed on molybdena but not vanadia catalysts. Our results suggest that decreasing the modulation frequency affects O_*/O_L ratios and ethylene selectivity values in a manner analogous to a reduction in residence time.

4. CONCLUSIONS

We show that forced dynamic operation can lead to higher ethylene selectivities during ethane ODH over MoO_x/Al_2O_3

https://doi.org/10.1021/acscatal.3c06066
ACS Catal. 2024, 14, 7877−7892

catalysts but not VO_x/Al_2O_3 catalysts, and establish a kinetic basis for the observed dynamic enhancement. Higher dynamic ethylene selectivity values over MoO_x catalysts are shown to result from undesired combustion reactions being more sensitive to O_2 concentration compared to the desired ODH reaction to produce ethylene. The lack of dynamic enhancement for VO_x catalysts, on the other hand, is interpreted as a consequence of the O_2 concentration independence of all three rates in the triangular reaction network. A reactor model employing a kinetic scheme accounting for two distinct types of oxygen species—chemisorbed (O_*) and lattice (O_L) oxygens—that carry distinct oxidation and reduction half cycle parameters indicates that whereas oxygen speciation affects the nature of hydrocarbon activated (ethane or ethylene) on VO_x/Al_2O_3, in the case of MoO_x/Al_2O_3 it affects the type of product formed (ethylene or CO_x). The O_2 concentration independence of rates on VO_x/Al_2O_3 are rationalized in terms of the much higher oxidation/reduction rate constant ratios compared to MoO_x catalysts that exhibit positive fractional orders in O_2.

We present the transient reactor-averaged ratio of chemisorbed to lattice oxygen (O_*/O_L ratio) as a salient variable that enables an interpretation of the choice of catalyst and reaction conditions under which dynamic enhancement is observed. For example, dynamic enhancement is more likely to be observed on catalysts carrying lower molybdena coverages because chemisorbed oxygens on these samples both (a) reoxidize at a slower rate, and (b) migrate to lattice positions at a faster rate compared to samples with higher molybdena coverages. Both these factors render MoO_x samples at low weight loadings to be amenable to minimizing reactor-averaged O_*/O_L ratios through dynamic modulation. VO_x catalysts, on the other hand, carry chemisorbed oxygen that is more similar in reducibility and reactivity to lattice oxygen, and this species reoxidizes and migrates at faster and slower rates, respectively, thereby limiting the practicability of improving selectivity through dynamic operation. Lastly, modulation frequency can be used to control the extent of dynamic enhancement, with changes at low frequency mimicking the effects that residence time has on selectivity-conversion behavior, and those at higher frequencies causing a convergence between SS and dynamic values owing to the shorter reduction half cycles resulting in a preclusion of transient O_*/O_L ratios low enough to observe an improvement in performance relative to SS conditions. By providing a quantitative kinetic interpretation of dynamic enhancement that is grounded in the identity and reactivity of oxygen species participating in MvK cycles, this study establishes a basis for rigorously identifying catalyst and reaction engineering markers for improving performance by employing dynamic reactor operation strategies that are currently attracting widespread attention in catalytic partial oxidation reactions specifically, and large-scale reaction systems more generally.

■ ASSOCIATED CONTENT

Supporting Information

The Supporting Information is available free of charge at https://pubs.acs.org/doi/10.1021/acscatal.3c06066.

Transport limitation calculations and tables, reactor setup, BET isotherms, XRD patterns, CO TPR, CO_x profiles, comparison between model and experiments, intracrystalline diffusion calculations, and apparent oxygen orders of the two-oxygen site model (PDF)

■ AUTHOR INFORMATION

Corresponding Authors

Michael P. Harold − *William A. Brookshire Department of Chemical and Biomolecular Engineering, Houston, Texas 77204-4004, United States*; Email: mpharold@central.uh.edu

Praveen Bollini − *William A. Brookshire Department of Chemical and Biomolecular Engineering, Houston, Texas 77204-4004, United States*; orcid.org/0000-0001-8092-8092; Email: ppbollini@uh.edu

Author

Austin Morales − *William A. Brookshire Department of Chemical and Biomolecular Engineering, Houston, Texas 77204-4004, United States*

Complete contact information is available at: https://pubs.acs.org/10.1021/acscatal.3c06066

Notes

The authors declare no competing financial interest.

■ ACKNOWLEDGMENTS

The authors acknowledge support from the National Science Foundation (EFMA 2029359).

■ SYMBOLS

C_i, concentration [μmol/cm^3]
F, volumetric flow rate [cm^3/min]
M, number of experiments/data points
N, number of species
N_i, moles of species i
S_i, carbon selectivity
X_i, conversion
T, temperature
R_i, rate [umol/min/mg cat]
RSS, sum of least-squares residuals
W, mass of catalyst [mg]
$a_\#$, rmpirical parameters of sigmoid function
a, b, c, apparent reaction orders (power law)
f, frequency [min^{-1}]
k, rate constant
s, duty cycle
t, time [min]

■ GREEK SYMBOLS

θ, normalized coverage (by total site density)
ρ_{cat}, catalyst density [mg cat/cm^3 reactor]
ε_{bed}, void fraction of catalyst bed
ν_i, number of carbons
τ, W/F [mg/sccm]

■ SUBSCRIPTS

exp, experimental
f, red, final time point of reduction half cycle
i, species name
L, lattice (oxygen)
model, model
ox, oxidation half cycle
red, reduction half cycle

https://doi.org/10.1021/acscatal.3c06066
ACS Catal. 2024, 14, 7877−7892

*, chemisorbed (oxygen)

SUPERSCRIPTS

f, feed
′, effective (rate constant for power law)

REFERENCES

(1) Gärtner, C. A.; van Veen, A. C.; Lercher, J. A. Oxidative dehydrogenation of ethane: Common principles and mechanistic aspects. *ChemCatChem* **2013**, *5*, 3196−3217.
(2) Najari, S.; Saeidi, S.; Concepcion, P.; Dionysiou, D. D.; Bhargava, S. K.; Lee, A. F.; Wilson, K. Oxidative dehydrogenation of ethane: catalytic and mechanistic aspects and future trends. *Chem. Soc. Rev.* **2021**, *50*, 4564−4605.
(3) Argyle, M. D.; Chen, K.; Bell, A. T.; Iglesia, E. Effect of catalyst structure on oxidative dehydrogenation of ethane and propane on alumina-supported vanadia. *J. Catal.* **2002**, *208*, 139−149.
(4) Argyle, M. D.; Chen, K.; Bell, A. T.; Iglesia, E. Ethane oxidative dehydrogenation pathways on vanadium oxide catalysts. *J. Phys. Chem. B* **2002**, *106*, 5421−5427.
(5) Gao, Y.; Neal, L. M.; Li, F. Li-Promoted $LaxSr_{2-x}FeO_{4-\delta}$ Core-Shell Redox Catalysts for Oxidative Dehydrogenation of Ethane under a Cyclic Redox Scheme. *ACS Catal.* **2016**, *6*, 7293−7302.
(6) Novotný, P.; Yusuf, S.; Li, F.; Lamb, H. H. Oxidative dehydrogenation of ethane using MoO3/Fe2O3 catalysts in a cyclic redox mode. *Catal. Today* **2018**, *317*, 50−55.
(7) Haddad, N.; Bordes-Richard, E.; Hilaire, L.; Barama, A. Oxidative dehydrogenation of ethane to ethene on alumina-supported molybdenum-based catalysts modified by vanadium and phosphorus. *Catal. Today* **2007**, *126* (1−2), 256−263.
(8) Luongo, G.; Donat, F.; Bork, A. H.; Willinger, E.; Landuyt, A.; Müller, C. R. Highly Selective Oxidative Dehydrogenation of Ethane to Ethylene via Chemical Looping with Oxygen Uncoupling through Structural Engineering of the Oxygen Carrier. *Adv. Energy Mater.* **2022**, *12*, 2200405.
(9) Yusuf, S.; Neal, L.; Haribal, V.; Baldwin, M.; Lamb, H. H.; Li, F. Manganese silicate based redox catalysts for greener ethylene production via chemical looping - oxidative dehydrogenation of ethane. *Appl. Catal., B* **2018**, *232*, 77−85.
(10) Bakare, I. A.; Mohamed, S. A.; Al-Ghamdi, S.; Razzak, S. A.; Hossain, M. M.; de Lasa, H. I. Fluidized bed ODH of ethane to ethylene over VO_x-MoO_x/γ-Al_2O_3 catalyst: Desorption kinetics and catalytic activity. *Chem. Eng. J.* **2015**, *278*, 207−216.
(11) Waku, T. D.; Argyle, M. D.; Bell, A.; Iglesia, E. Effects of O_2 Concentration on the Rate and Selectivity in Oxidative Dehydrogenation of Ethane Catalyzed by Vanadium Oxide: Implications for O2 Staging and Membrane Reactors. *Ind. Eng. Chem. Res.* **2003**, *42*, 5462−5466.
(12) Skoufa, Z.; Heracleous, E.; Lemonidou, A. A. Investigation of engineering aspects in ethane ODH over highly selective $Ni_{0.85}Nb_{0.15}O_x$ catalyst. *Chem. Eng. Sci.* **2012**, *84*, 48−56.
(13) Brody, L.; Neal, L.; Liu, J.; Li, F. Autothermal Chemical Looping Oxidative Dehydrogenation of Ethane: Redox Catalyst Performance, Longevity, and Process Analysis. *Energy Fuels* **2022**, *36*, 9736−9744.
(14) Chen, J.; Sun, Z.; Bollini, P.; Balakotaiah, V. Scale-up analysis of the oxidative dehydrogenation of ethane over MoVTeNbOx catalysts in an autothermal reactor. *Chem. Eng. Sci.* **2023**, *273*, 118649.
(15) Gabra, S.; Baldoví, H. G.; Williams, G.; Poulston, S.; Dennis, J. MoVNbTeO for chemical looping-oxidative dehydrogenation of ethane. *AIChE Annual Meeting, Conference Proceedings*, 2019.
(16) Dinse, A.; Schomäcker, R.; Bell, A. T. The role of lattice oxygen in the oxidative dehydrogenation of ethane on alumina-supported vanadium oxide. *Phys. Chem. Chem. Phys.* **2009**, *11*, 6119−6124.
(17) Haber, J.; Turek, W. J. Kinetic Studies as a Method to Differentiate between Oxygen Species Involved in the Oxidation of Propene. *Catalysis* **2000**, *190*, 320−326.
(18) Neal, L. M.; Yusuf, S.; Sofranko, J. A.; Li, F. Oxidative Dehydrogenation of Ethane: A Chemical Looping Approach. *Energy Technol.* **2016**, *4*, 1200−1208.
(19) Novotný, P.; Yusuf, S.; Li, F.; Lamb, H. H. MoO_3/Al_2O_3 catalysts for chemical-looping oxidative dehydrogenation of ethane. *J. Chem. Phys.* **2020**, *152*, 044713.
(20) López, E.; Heracleous, E.; Lemonidou, A. A.; Borio, D. O. Study of a multitubular fixed-bed reactor for ethylene production via ethane oxidative dehydrogenation. *Chem. Eng. J.* **2008**, *145*, 308−315.
(21) Harold, M. P.; Zaspalis, V. T.; Keizer, K.; Burggraaf, A. J. Intermediate product yield enhancement with a catalytic inorganic membrane—I. Analytical model for the case of isothermal and differential operation. *Chem. Eng. Sci.* **1993**, *48*, 2705−2725.
(22) Huang, X.-F.; Li, C.-Y.; Chen, B.-H.; Silveston, P. L. Transient kinetics of n-Butane oxidation to maleic anhydride over a VPO catalyst. *AIChE J.* **2002**, *48*, 846−855.
(23) van der Linde, S. C.; Nijhuis, T. A.; Dekker, F. H. M.; Kapteijn, F.; Moulijn, J. A. Mathematical treatment of transient kinetic data: Combination of parameter estimation with solving the related partial differential equations. *Appl. Catal. A* **1997**, *151*, 27−57.
(24) Bhore, N. A.; Klein, M. T.; Bischoff, K. B. The Delplot Technique: A New Method for Reaction Pathway Analysis. *Ind. Eng. Chem. Res.* **1990**, *29*, 313−316.
(25) Christodoulakis, A.; Boghosian, S. Molecular structure and activity of molybdena catalysts supported on zirconia for ethane oxidative dehydrogenation studied by operando Raman spectroscopy. *J. Catal.* **2008**, *260*, 178−187.
(26) Yao, R.; Herrera, J. E.; Chen, L.; Chin, Y. H. C. Generalized Mechanistic Framework for Ethane Dehydrogenation and Oxidative Dehydrogenation on Molybdenum Oxide Catalysts. *ACS Catal.* **2020**, *10*, 6952−6968.
(27) Ting, A. W. L.; Li, M.; Harold, M. P.; Balakotaiah, V. Fast cycling in a non-isothermal monolithic lean NO_x trap using H_2 as reductant: Experiments and modeling. *Chem. Eng. J.* **2017**, *326*, 419−435.
(28) Ressler, T.; Wienold, J.; Jentoft, R. E.; Neisius, T. Bulk structural investigation of the reduction of MoO_3 with propene and the oxidation of MoO_2 with oxygen. *J. Catal.* **2002**, *210*, 67−83.
(29) Clair, T. P. S.; Restad, J. M.; Oyama, S. T. Oxygen diffusivity in MoO_3 as determined by a temperature programmed method. *J. Mater. Res.* **1998**, *13*, 1430−1433.
(30) Zhou, Z.; Harold, M. P.; Luss, D. Dynamic oxygen storage capacity of ceria-zirconia and Mn0.5Fe2.5O4Spinel: Experiments and modeling. *Ind. Eng. Chem. Res.* **2021**, *60*, 6465−6482.
(31) Heracleous, E.; Lee, A. F.; Vasalos, I. A.; Lemonidou, A. A. Surface properties and reactivity of Al2O3-supported MoO3 catalysts in ethane oxidative dehydrogenation. *Catal. Lett.* **2003**, *88*, 47−53.
(32) Tsilomelekis, G.; Christodoulakis, A.; Boghosian, S. Support effects on structure and activity of molybdenum oxide catalysts for the oxidative dehydrogenation of ethane. *Catal. Today* **2007**, *127*, 139−147.
(33) Elbadawi, A. H.; Ba-Shammakh, M. S.; Al-Ghamdi, S.; Razzak, S. A.; Hossain, M. M. Reduction kinetics and catalytic activity of VO_x/γ-Al_2O_3-ZrO_2 for gas phase oxygen free ODH of ethane. *Chem. Eng. J.* **2016**, *284*, 448−457.
(34) Khodakov, A.; Yang, J.; Su, S.; Iglesia, E.; Bell, A. T. Structure and Properties of Vanadium Oxide-Zirconia Catalysts for Propane Oxidative Dehydrogenation. *J. Catal.* **1998**, *177*, 343−351.
(35) Kanervo, J. M.; Harlin, M. E.; Krause, A. I.; Bañares, M. A. Characterisation of alumina-supported vanadium oxide catalysts by kinetic analysis of H2-TPR data. *Catal. Today* **2003**, *78*, 171−180.
(36) Schwarz, O.; Frank, B.; Hess, C.; Schomäcker, R. Characterisation and catalytic testing of VO_x/Al_2O_3 catalysts for microstructured reactors. *Catal. Commun.* **2008**, *9*, 229−233.
(37) Frank, B.; Dinse, A.; Ovsitser, O.; Kondratenko, E. v.; Schomäcker, R. Mass and heat transfer effects on the oxidative dehydrogenation of propane (ODP) over a low loaded VOx/Al2O3 catalyst. *Appl. Catal., A* **2007**, *323*, 66−76.

https://doi.org/10.1021/acscatal.3c06066
ACS Catal. 2024, 14, 7877−7892

(38) Redlingshöfer, H.; Fischer, A.; Weckbecker, C.; Huthmacher, K.; Emig, G. Kinetic Modeling of the Heterogeneously Catalyzed Oxidation of Propene to Acrolein in a Catalytic Wall Reactor. *Ind. Eng. Chem. Res.* **2003**, *42*, 5482−5488.
(39) Blasco, T.; Galli, A.; López Nieto, J.; Trifiró, F. Oxidative dehydrogenation of ethane and n-butane on VOx/Al2O3 catalysts. *J. Catal.* **1997**, *169*, 203−211.
(40) Martinezhuerta, M.; Gao, X.; Tian, H.; Wachs, I. E.; Fierro, J. L. G.; Banares, M.; Sánchez, F. Oxidative dehydrogenation of ethane to ethylene over alumina-supported vanadium oxide catalysts: Relationship between molecular structures and chemical reactivity. *Catal. Today* **2006**, *118*, 279−287.
(41) Kapoor, R.; Oyama, S. T. Measurement of solid state diffusion coefficients by a temperature-programmed method. *J. Mater. Res.* **1997**, *12*, 467−473.
(42) Heracleous, E.; Lemonidou, A. A. Reaction pathways of ethane oxidative and non-oxidative dehydrogenation on γ-Al_2O_3 studied by temperature-programmed reaction (TP-reaction). *Catal. Today* **2006**, *112*, 23−27.
(43) Skoufa, Z.; Heracleous, E.; Lemonidou, A. A. On ethane ODH mechanism and nature of active sites over NiO-based catalysts via isotopic labeling and methanol sorption studies. *J. Catal.* **2015**, *322*, 118−129.
(44) Sinčić, D.; Bailey, J. E. Analytical optimization and sensitivity analysis of forced periodic chemical processes. *Chem. Eng. Sci.* **1980**, *35*, 1153−1161.
(45) Silveston, P. L.; Hudgins, R. R. *Periodic Operation of Chemical Reactors*; Elsevier Science, 2013.
(46) Silveston, P.; Hudgins, R. R.; Renken, A. Periodic operation of catalytic reactors-introduction and overview. *Catal. Today* **1995**, *25*, 91−112.
(47) Lee, C. K.; Bailey, J. E. Modification of Consecutive-Competitive Reaction Selectivity by Periodic Operation. *Ind. Eng. Chem. Process Des. Dev.* **1980**, *19*, 160−166.
(48) Cho, B. K. Dynamic Behavior of a Single Catalyst Pellet. 1. Symmetric Concentration Cycling during CO Oxidation over Pt/Al_2O_3. *Ind. Eng. Chem. Fundam.* **1983**, *22*, 410−420.
(49) Petkovska, M.; Nikolić, D.; Seidel-Morgenstern, A. Nonlinear Frequency Response Method for Evaluating Forced Periodic Operations of Chemical Reactors. *Isr. J. Chem.* **2018**, *58* (6−7), 663−681.
(50) Sterman, L. E.; Erik Ydstie, B. The steady-state process with periodic perturbations. *Chem. Eng. Sci.* **1990**, *45*, 721−736.

https://doi.org/10.1021/acscatal.3c06066
ACS Catal. 2024, 14, 7877−7892